Npas1^{+}-Nkx2.1^{+} Neurons Form A Unique Pallidal Neuron Subclass

Zachary A. Abecassis[1]*, Brianna L. Berceau[1]*, Jeff P. Win[1], Daniela Garcia[1], Harry S. Xenias[1], Qiaoling Cui[1], Arin Pamucku[1], Vivian M. Hernández[1], Uree Chon[2], Byungkook Lim[3], Yongsoo Kim[2], Nicholas J. Justice[4], Raj Awatramani[5], C. Savio Chan[1]

[1] Department of Physiology, Feinberg School of Medicine, Northwestern University, Chicago, IL, USA

[2] Department of Neural and Behavioral Sciences, College of Medicine, Penn State University, Hershey, PA, USA

[3] Neurobiology Section, Biological Sciences Division, University of California San Diego, La Jolla, CA, USA

[4] Institute of Molecular Medicine, University of Texas, Houston, TX USA

[5] Department of Neurology, Feinberg School of Medicine, Northwestern University, Chicago, IL, USA

(*equal contributions)

Correspondence should be addressed to C. Savio Chan, Department of Physiology, Feinberg School of Medicine, Northwestern University, 303 East Chicago Avenue, Chicago, IL 60611. saviochan@gmail.com

Acknowledgments

This work is supported by NIH R01 NS069777 (CSC), P50 NS047085 (CSC), R01 MH112768 (CSC), R01 NS097901 (CSC), R01 MH109466 (CSC), R01 NS088528 (CSC), R01 NS096240 (RA), R21 NS072703 (RA), R01 MH110556 (RA), P30 CA060553 (RA), R01 MH107742 (BL), R01 MH108594 (BL), U01 MH114829 (BL), R01 MH116176 (YK), R01 MH112768 (NJJ), T32 NS041234 (HSX), F32 NS098793 (HSX), T32 AG020506 (AP), HHMI-PF Medical Research Fellowship (ZA), ΑΩΑ Student Research Fellowship (ZA) and Northwestern University Weinberg Summer Research Grant (JW). We thank Suraj Cherian, Xixun Du, Elizabeth Augustine, and Daniel Hegeman for their assistance on the project, Alexandria Granados, Morgan Marshall, and Nicole Curtis, for colony management and technical support, Northwestern University Transgenic and Targeted Mutagenesis Laboratory for providing EIIa-Cre and CAG-Flp breeders.

Author contributions

ZAA and BLB conceived the study. ZAA, HSX, QC, AP, and VMH conducted and analyzed the electrophysiological measurements. DG, JPW, ZAA, QC, UC, BL, and YK performed and analyzed the tracing studies. BLB performed the immunohistological experiments. JPW performed cell counts and generated spatial maps with help from HSX. NJJ provided unpublished data that led to the proposed classification scheme. RA provided essential tools and expertise on fate-mapping. BLB led the writing of the manuscript. CSC directed and supervised the project. All authors reviewed and edited the manuscript.

Abstract (237 words)

Within the basal ganglia circuit, the GPe is critically involved in motor control. Aside from Foxp2$^+$ neurons and ChAT$^+$ neurons that have been established as unique neuron types, there is no consensus on the classification of GPe neurons. Properties of the remaining neuron types are poorly defined. In this study, we leverage new mouse lines, viral tools, and molecular markers to study GPe neurons. By examining multiple modalities, we sought to better define GPe neuron subtypes. We found that Sox6 represents a novel, defining marker for GPe neuron subtypes. Lhx6$^+$ neurons that lack the expression of Sox6 were devoid of both parvalbumin and Npas1. This result confirms previous assertions of the existence of a unique Lhx6$^+$ population. Neurons that arise from the Dbx1$^+$ lineage were similarly abundant in the GPe and displayed a heterogeneous makeup. Tracing experiments revealed that Npas1$^+$-Nkx2.1$^+$ neurons represent the principal, non-cholinergic, cortically-projecting neurons; they project profusely in the cortex and are part of a cortico-pallidal-cortical loop. Lastly, analysis of the spatial distribution and electrophysiological properties of a number of GPe neuron types further confirms the diversification of GPe subtypes. In summary, we provide improved descriptions of GPe neuron subtypes. By delineating different GPe neurons and their synaptic partners, our findings establish the circuit substrates that can be important for motor function and dysfunction. Our findings reconcile some of the discrepancies that arose from differences in techniques or the reliance on pre-existing tools.

Significant statement (125 words)

The poor understanding of the neuronal composition in the GPe undermines our ability to interrogate its precise behavioral and disease involvements. We sought to provide a more comprehensive description of the neuron composition in the adult mouse GPe by leveraging a powerful set of tools. Here, nine different genetic crosses were used, 370 neurons were electrophysiologically-characterized, and over 100,000 neurons were histologically- and/or anatomically-profiled. Our current study further illustrates the complexity of GPe neurons in adult mice and infers the existence of new neuron subclasses. In particular, our results support the idea that Npas1^{+}-Nkx2.1^{+} neurons are a distinct GPe neuron subclass. Our results glean new insights into the cellular and circuit substrates for motor function and dysfunction.

Introduction (496 words)

The basal ganglia are a network of brain nuclei that are involved in motor control and adaptive behavior. Dysfunction within this circuit can be devastating, as seen in patients afflicted by Parkinson's Disease (PD), Huntington's Disease, and dystonias (DeLong and Wichmann, 2007; Graybiel, 2008; Ito and Doya, 2011; Jahanshahi et al., 2015; Klaus et al., 2019; Mink, 1996; Nambu and Tachibana, 2014; Redgrave et al., 2010). The external globus pallidus (GPe) is a key nucleus within the basal ganglia. Decorrelated, phasic changes in GPe neuron activity are observed with normal movements (Anderson and Horak, 1985; Dodson et al., 2015; Jin et al., 2014; Mallet et al., 2016; Shi et al., 2004; Turner and Anderson, 2005). Alterations in the firing pattern of these neurons are associated with hypokinetic motor symptoms in both animal models of PD and human patients (Hegeman et al., 2016; Jaeger and Kita, 2011).

Prior studies in the field have suggested GPe neuron subtypes are involved in some aspect of movement control (Dodson et al., 2015; Glajch et al., 2016; Mastro et al., 2017). However, precisely how these neuron subclasses are involved in motor function and dysfunction is poorly defined. Our past work characterized two principal classes of GPe neurons, parvalbumin-expressing (PV^+) neurons and Npas1-expressing ($Npas1^+$) neurons, which account for 55% and 27% of the GPe neurons, respectively. PV^+ neurons project primarily to the subthalamic nucleus (STN) and $Npas1^+$ neuron target the dorsal striatum (dStr). The $Npas1^+$ population can be further broken down into distinct Foxp2-expressing ($Foxp2^+$) and Nkx2.1-expressing ($Nkx2.1^+$) subpopulations, with $Foxp2^+$ neurons representing a unique population referred to as "arkypallidal" neurons (Abdi et al., 2015; Dodson et al., 2015; Hernandez et al., 2015). GPe neurons lacking Foxp2 expression, commonly referred to as "prototypic" neurons, are a more heterogeneous population. As we lack a complete description of the molecular identity of prototypic neurons, the precise function of prototypic neurons has not been systematically studied.

Lhx6-expressing ($Lhx6^+$) neurons represent a substantial fraction of the prototypic GPe neuron subtype, although their reported abundance varies widely across laboratories (Abrahao and Lovinger, 2018; Dodson et al., 2015; Hernandez et al., 2015; Mastro et al., 2014). Unfortunately, due to limitations in the availability of a reliable transgenic mouse and antibodies to study this subset, a discrepancy remains in its abundance and extent of

overlap with PV$^+$ neurons and Npas1$^+$ neurons across laboratories (Hegeman et al., 2016). In this study, we hypothesize the existence of a unique Lhx6$^+$ GPe population that corresponds to the PV$^-$ and Npas1$^-$ (PV$^-$-Npas1$^-$) neurons we previously identified and accounts for ~15–20% of the total GPe neuron population (Hernandez et al., 2015). These neurons could play an important role in neural function if they target a unique brain area, such as the cortex, which has been described recently (Ahrlund-Richter et al., 2019; Chen et al., 2015; Saunders et al., 2015; Schwarz et al., 2015). With the advent of additional transgenic lines and viruses, we used molecular marker expression and connectome analysis to reconcile discrepancies and provide a more in-depth analysis of the neuronal makeup and its diversity within the GPe. We confirmed the existence of a unique Lhx6$^+$ neuron population by its lack of Sox6 expression. This Lhx6$^+$ population does not correspond to neurons that arise from the Dbx1-lineage, which is known to colonize the GPe. We found that Npas1$^+$-Nkx2.1$^+$ neurons represent the principal, non-cholinergic, cortically-projecting population, and they are part of a closed-loop formed between cortex and the GPe. We propose that Npas1$^+$-Nkx2.1$^+$ neurons, along with the previously identified Npas1$^+$-Foxp2$^+$ and ChAT$^+$ neurons, are unique GPe neuron types.

Materials and Methods

Mice

All procedures were done in accordance with protocols approved by Northwestern University and the University of California, San Diego Institutional Animal Care and Use Committees and were in compliance with the National Institutes of Health Guide to the Care and Use of Laboratory Animals. Experiments were conducted with the following mouse lines: LSL(Lox-STOP-Lox)-tdTomato (Ai14, Jax 007914), FSF(Frt-STOP-Frt)-LSL-tdTomato (Ai65, Jax 021875). Dbx1-ires-Cre mice (MMRRC 031751) (Harris et al., 2014) were crossed with LSL-tdTomato. As the Dbx1-ires-Cre line is prone to germline recombination, recombination patterns were routinely monitored and compared against data on Allen's Transgenic Characterization data portal (http://connectivity.brain-map.org/transgenic/experiment/100141723). Any mice displaying ectopic expression were excluded from subsequent analysis. Foxp2-ires-Cre (Jax 030541), Nkx2.1-ires-Flp (Jax 028577), Npas1-Cre-tdTomato BAC (Jax 027718), PV-ires-Cre (Jax 017320), PV-2A-Flp (Jax 022730), PV-tdTomato BAC (Jax 027395). FSF-tdTomato (Ai65F) was generated as previously described (Daigle et al., 2018; Yetman et al., 2019). In brief, FSF-LSL-tdTomato was crossed with EIIa-Cre (Jax 003724) to delete the LSL cassette. Sox6-Cre was generated by performing a germline deletion of the FSF cassette from our previously reported Sox6-FSF-Cre (Poulin et al., 2018), using CAG-Flp (Kanki et al., 2006) line. Dbx1;Ai14 referred to as Dbx1-L-tdTom. Nkx2.1-Flp;Ai65 referred to as Nkx2.1-F-tdTom. PV-Cre;Ai14 referred to as PV-L-tdTom. PV-Flp;Ai65F referred to as PV-F-tdTom. PV-Flp;Dbx1-Cre;Ai65 referred to as PV-Dbx1-FL-tdTom. Mice were backcrossed and only heterozygous and hemizygous mice were used throughout the study to minimize the potential alteration of the phenotypes in mice carrying the transgene alleles (Chan et al., 2012). Mice were group-housed in a 12 h light-dark cycle. Food and water were provided *ad libitum*. All mice were maintained by backcrossing with C57BL/6J breeders (Jax 000664). The genotypes of all transgenic mice were determined by tail biopsy followed by PCR to identify the presence of the relevant transgenes. Both male and female mice were used in this study.

Stereotaxic injections

Standard injection procedures were used as described previously (Cui et al., 2016). In brief, mice at postnatal days 28–35 and 45–55 were used for viral tracing and retrograde tracing experiments, respectively, were anesthetized with isoflurane, and were immobilized on a stereotaxic frame (David Kopf Instruments). A small craniotomy (~1 mm diameter) was made with a dental drill (Osada) for injection into the target (see **Table 1**) using a calibrated glass micropipette (VWR) at a rate of 0.3–0.5 µl/min. The micropipette was left *in situ* for 5–10 min post injection to maximize viral retention and to decrease capillary spread upon pipette withdrawal. The following adeno-associated viruses (AAVs) were used in this study: AAV-EF1a-CreOn-hChR2(H134R)-EYFP (Addgene viral prep #20298-AAV9) and AAV-hSyn-CreOn-mCherry (Addgene viral prep #50459-AAV8). Mice injected with Alexa-conjugated cholera-toxin B subunit (CTb; Thermo Fisher Scientific), lentivirus (LV, RG-EIAV-CAG-Cre; UCSD) (Knowland et al., 2017), or AAVs were processed for immunohistological analysis (see below) 7–14 d and 28–42 d after injection, respectively. For LV tracing experiments, CTb was injected in conjunction with LV to visualize targeting accuracy. Mice with injection outside of the targeted area were excluded from subsequent analysis.

Immunolabeling and quantification

Mice ranging in age from postnatal day 55–80 were anesthetized deeply with a ketamine-xylazine mixture and perfused transcardially first with phosphate-buffered saline (PBS) followed by fixative containing 4% paraformaldehyde (PFA, pH 7.4). Tissue was then postfixed in the same fixative for 2 h at 4 ºC. Tissue blocks containing the GPe were sectioned using a vibrating microtome (Leica Instruments) at a thickness of 60 µm. Floating sections were blocked with 10% (v/v) normal goat or donkey serum (Thermo Fisher Scientific) and 0.2% (v/v) Triton X-100 in PBS for 30–60 min, and were subsequently incubated with primary antibodies (see **Table 2**) in the same solution for 16–24 h at 4 ºC. After washes in PBS, the sections were incubated with Alexa-conjugated IgG antibody (Thermo Fisher Scientific, 1:500 dilution) at room temperature for 2 h. The sections were then washed, mounted with ProLong Antifade mounting medium (Thermo Fisher Scientific), and coverslipped. In a subset of the experiments, DAPI was used to delineate cytoarchitecture of different brain structures. Fluorescent images of injection sites were captured on an epifluorescence microscope (Keyence Corporation) using a 2x or

10× 0.45 numerical aperture (NA) objective. Immunoreactivity in neurons was examined on a laser-scanning confocal microscope (Olympus). For cell quantification, images of the entire GPe were acquired on a laser-scanning confocal microscope with a 60× 1.35 NA oil-immersion objective. Images encompassing the GPe were taken and stitched using FLUOVIEW Viewer (Olympus) or Photoshop CC (Adobe Systems). Cell counting was performed with Fiji (Schindelin et al., 2012) using a cell counter plugin. Cell counts were obtained from ~28 optical sections that were captured at 1 µm increments (median = 28). Neurons were defined by cells that were immuno-positive for HuCD (Hernandez et al., 2015). GPe sections from three different equally-spaced (400 µm) lateromedial levels (~2.5, 2.1, and 1.7 mm from bregma) were sampled and assigned as lateral, intermediate, and medial, respectively (Hernandez et al., 2015). They correspond approximately to sagittal plate 7, 9, and 11 on the Allen reference atlas (http://mouse.brain-map.org/static/atlas). In this study, the GPe is considered to be the structure that spans between the dorsal striatum and the internal capsule, which define the rostral and caudal and borders of the GPe on a sagittal plane, respectively. The cytoarchitecture of the ventral border is more ambiguous. For consistency, six non-overlapping z-stacks (212.13 x 212.13 µm) traversing the long axis of the GPe were used to capture its dorsoventral extent. This strategy coincides with the ventral border demarcated by the dense astrocytic labeling in the Dbx1-L-tdTom mice (see Results) and that defined in the common reference atlas.

To mathematically represent the spatial distribution of GPe neurons and to compare that across neuron populations, sagittal brain sections were histologically processed. Images were manually aligned to the Allen Reference Atlas based on the structural information across the entire brain section. Images were transformed linearly (i.e. rotation, scaling) with no warping algorithms applied. Neurons that were not present within the confines of the GPe in the reference atlas were removed from subsequent analysis. GPe neurons located at lateral, intermediate, and medial levels (~2.5, 2.1, and 1.7 mm lateral from bregma) were charted and collapsed onto a single sagittal plane. The location of each neuron was then defined by its x-y coordinates. To capture the aggregate spatial distribution, a geometric centroid of each neuron population was then determined to represent

the center of mass in both x and y dimensions. Centroids were then used as the origin for the polar histograms. The size of each sector represents the relative neuron count as a function of direction.

Serial two-photon tomography

Serial two-photon tomography was used to map input to the GPe from the entire cortex. Imaging and analysis were performed as previously described (Kim et al., 2017). Two weeks after LVretro-Cre and CTb-488 injection, mouse brains were fixed as described above. Brains were then transferred to PBS and stored at 4 °C until imaged. Brains were embedded in 4% agarose in 0.05 M phosphate buffer and cross-linked in 0.2% sodium borohydrate solution (in PBS, pH 9.0–9.5). Each brain was imaged with a high-speed two-photon microscope with integrated vibratome (TissueVision) at 1 µm at both x-y resolution with 280 z-sections in every 50 µm. A 910-nm two-photon laser (Coherent) was used for CTb488 and tdTomato excitation. A dichroic mirror (Chroma) and band pass filters (Semrock) were used to separate green and red fluorescence signals. Emission signals were detected by GaAsP photomultiplier tubes (Hamamatsu). An automated, whole-brain cell counting and registration of the detected signal on a reference brain was applied as described before (Kim et al., 2017). The number of tdTomato$^+$ neurons from each brain region was charted. The relative size of input to the GPe was calculated by normalizing the total number of tdTomato$^+$ neurons in the entire brain of each sample.

Visualized *ex vivo* electrophysiology

Mice in the age range postnatal day 55–90 were anesthetized with a ketamine-xylazine mixture and perfused transcardially with ice-cold aCSF containing the following (in mM): 125 NaCl, 2.5 KCl, 1.25 NaH_2PO_4, 2.0 $CaCl_2$, 1.0 $MgCl_2$, 25 $NaHCO_3$, and 12.5 glucose, bubbled continuously with carbogen (95% O_2 and 5% CO_2). The brains were rapidly removed, glued to the stage of a vibrating microtome (Leica Instrument), and immersed in ice-cold aCSF. Parasagittal slices containing the dStr and the GPe were cut at a thickness of 240 µm and transferred to a holding chamber where they were submerged in aCSF at 35 ºC for 30 min and returned to room temperature for recording. Slices were then transferred to a small-volume (~0.5 ml) Delrin recording chamber that was mounted on a fixed-

stage, upright microscope (Olympus). Neurons were visualized using differential interference contrast optics (Olympus), illuminated at 735 nm (Thorlabs), and imaged with a 60× water-immersion objective (Olympus) and a CCD camera (QImaging). Genetically-defined neurons were identified by somatic eGFP or tdTomato fluorescence examined under epifluorescence microscopy with a daylight (6500 K) LED (Thorlabs) and appropriate filters (Semrock).

Recordings were made at room temperature (20–22 ºC) with patch electrodes fabricated from capillary glass (Sutter Instrument) pulled on a Flaming-Brown puller (Sutter Instrument) and fire polished with a microforge (Narishige) immediately before use. Pipette resistance was typically ~2–4 MΩ. For cell-attached and current-clamp recordings, the internal solution consisted of the following (in mM): 135 $KMeSO_4$, 10 Na_2phosphocreatine, 5 KCl, 5 EGTA, 5 HEPES, 2 Mg_2ATP, 0.5 $CaCl_2$, and 0.5 Na_3GTP, with pH adjusted to 7.25–7.30 with KOH. The liquid junction potential for this internal solution was ~7 mV and was not corrected. Stimulus generation and data acquisition were performed using an amplifier (Molecular Devices), a digitizer (Molecular Devices), and pClamp (Molecular Devices). For current-clamp recordings, the amplifier bridge circuit was adjusted to compensate for electrode resistance and was subsequently monitored. The signals were filtered at 1 kHz and digitized at 10 kHz. $KMeSO_4$ and Na_2-GTP were from ICN Biomedicals and Roche, respectively. All other reagents were obtained from Sigma-Aldrich.

For optogenetic experiments, blue excitation wavelength (peak, ~450 nm) from two daylight (6500 K) LEDs (Thorlabs) was delivered to the tissue slice from both a 60× water immersion objective and a 0.9 numerical aperture air condenser with the aid of 520 nm dichroic beamsplitters (Semrock). Light delivery was made at the site of electrophysiological recordings with a field of illumination of 500–700 µm in diameter. Paired pulse optogenetic activation of terminals was at 20 Hz with a light duration of 2 ms.

Experimental design and statistical analyses

Graphing and statistical analyses were performed with MATLAB (MathWorks) and Prism (GraphPad). Custom analysis codes are available on GitHub (https://github.com/chanlab). Sample size (*n* value) is defined by the

number of observations (i.e., neurons, sections). No statistical method was used to predetermine sample size. Data in the main text are presented as median values ± median absolute deviations (MADs) as measures of central tendency and statistical dispersion, respectively. Box plots are used for graphic representation of population data (Krzywinski and Altman, 2014; Streit and Gehlenborg, 2014). The central line represents the median, the box edges represent the interquartile ranges, and the whiskers represent 10–90th percentiles. Normal distributions of data were not assumed. Comparisons for unrelated samples were performed using Mann–Whitney *U* test at a significance level (α) of 0.05. Unless <0.0001, exact *P* values (two-tailed) are reported.

Results

PV$^+$ and Npas1$^+$ neurons are distinct GPe neuron classes

Our laboratory and others have shown previously that the GPe contains two near-exclusive, classes of principal neurons. They are distinguished by their respective expression of PV and Npas1 (Hegeman et al., 2016). However, the reported abundance of PV$^+$ neurons across laboratories ranges from 30–60%, and their overlap with Npas1$^+$ neurons within the GPe varies widely in the literature Abdi et al. (2015); (Abrahao and Lovinger, 2018; Dodson et al., 2015; Flandin et al., 2010; Mastro et al., 2014; Nobrega-Pereira et al., 2010; Oh et al., 2017; Saunders et al., 2015). As multiple mouse lines and well-characterized antibodies are available to study PV$^+$ neurons, we sought to re-evaluate the abundance of PV$^+$ GPe neurons and reconcile the inconsistencies. First, we examined PV immunoreactivity (PV-ir) across all GPe neurons using HuCD as a neuronal marker; we observed PV-ir in ~50% of GPe neurons (49 ± 4%, n = 2,726 neurons, 19 sections) (**Figure 1**). Four PV antibodies were used throughout the study (see **Table 2**). All PV antibodies yielded similar results and were therefore pooled. While both PV-tdTom BAC and PV-L-tdTom (PV-Cre;LSL-tdTomato) have been used consistently across laboratories for the identification of PV$^+$ neurons, the utility of the PV-Flp line for studies of GPe neurons has not been established. To harness the potential of this mouse line, we crossed it with a Flp-reporter (FSF-tdTomato) line (see Materials and Methods). The resultant PV-F-tdTom (PV-Flp;FSF-tdTomato) line produced robust, cytoplasmic neuron labeling similar to that of the PV-L-tdTom and PV-tdTom BAC lines. As expected, the PV-F-tdTom line showed prominent tdTomato-expression (tdTomato$^+$) not only in GPe PV$^+$ neurons but also in PV$^+$ neurons in the thalamic reticular nucleus (TRN) (**Figure 1**), cerebellum, and in PV$^+$ interneurons throughout the cortex, hippocampus, and striatum.

Close examination of the abundance of tdTomato$^+$ neurons across PV-tdTom BAC, PV-L-tdTom, and PV-F-tdTom lines all converge to ~50% of the total GPe neuron population (PV-tdTom BAC, 50 ± 9%, n = 571 neurons, 5 sections; PV-L-tdTom, 50 ± 13%, n = 878 neurons, 9 sections; PV-F-tdTom, 53 ± 15%, n = 859 neurons, 6 sections) (see **Table 2**). Comparison of tdTomato expression with PV-ir across all three transgenic lines demonstrated faithful reporting of PV$^+$ neurons (PV-tdTom BAC, 100 ± 0%, n = 742 out of 747 neurons, 6 sections; PV-L-tdTom,

100 ± 0%, *n* = 1,380 out of 1,392 neurons, 12 sections; PV-F-tdTom, 100 ± 0%, *n* = 930 out of 1,023 neurons, 6 sections).

The Npas1-Cre-tdTom line was previously generated in our laboratory, and it labels roughly 90% (88 ± 7%, *n* = 505 neurons) of neurons that endogenously express Npas1 in the GPe (Hernandez et al., 2015). As this mouse line does not fully capture all Npas1$^+$ neurons, we focused our quantifications on Npas1-immunoreactivity (Npas1-ir) with our previously characterized Npas1 antibodies (Hernandez et al., 2015). We found that Npas1$^+$ neurons make up ~30% (32 ± 4%, *n* = 3,361 neurons, 21 sections) of the GPe. This result is consistent with our previous quantification of 27% (27 ± 4%, *n* = 2,464 neurons), which accounts for the ~12% not captured by the Npas1 mouse. A re-evaluation of the overlap between PV and Npas1 confirmed our prior observation (Hernandez et al., 2015) that these two markers are expressed in almost completely segregated neuron populations. We observed a very low level of overlap across lateromedial GPe levels (2 ± 2%, *n* = 96 out of 1,777 neurons, 12 sections), with the most overlap observed at the intermediate level (lateral: 1 ± 1%, *n* = 17 neurons, 3 sections; intermediate: 3 ± 1%, *n* = 68 neurons, 5 sections; medial: 0 ± 0%, *n* = 11 neurons, 4 sections). This is slightly higher than our previous estimate and is likely related to our previous reliance on the Npas1 mouse line for quantification (Hernandez et al., 2015). Our data are at odds with Abrahao et al. (Abrahao and Lovinger, 2018), which shows a much higher (up to 12.6%) overlap between PV and Npas1 expression in the GPe.

Nkx2.1-F-tdTom mice label prototypic GPe neurons

With our current data on the neuronal subtypes of the GPe showing that PV accounts for 49%, Npas1 for 32%, and a small population of neurons expressing a cholinergic neuron marker, choline acetyltransferase (ChAT) (6 ± 2%, *n* = 267 neurons, 9 sections) (see **Table 3**), around 15% of the GPe population remains to be identified. While Lhx6$^+$ neurons overlap substantially with both PV$^+$ neurons and Npas1$^+$ neurons (Hernandez et al., 2015), we hypothesize that a subset of Lhx6$^+$ neurons may correspond to that 15% of GPe neurons that are PV$^-$ and Npas1$^-$

.

As the use of the Lhx6-GFP mouse line resulted in highly inconsistent results across laboratories (Hegeman et al., 2016), we decided to systematically examine the expression of Nkx2.1 and Sox6 in GPe neurons. This was motivated by the observation that Nkx2.1, Lhx6, and Sox6 work in concert to control the fate of forebrain GABAergic neurons (Batista-Brito et al., 2009; Du et al., 2008; Jaglin et al., 2012). By examining the expression patterns of the signaling molecules that are upstream and downstream of Lhx6 (i.e. Nkx2.1 and Sox6, respectively), we sought to glean insights into an improved GPe neuron classification. Consistent with the fact that Nkx2.1 plays a crucial role in GPe development (Flandin et al., 2010; Nobrega-Pereira et al., 2010; Rubenstein et al., 1998; Sussel et al., 1999), Nkx2.1 immunolabeling revealed that ~60% (60 ± 2%, *n* = 5,342 neurons, 16 sections) of GPe neurons are Nkx2.1-expressing (Nkx2.1$^+$) (**Figure 1, Table 3**). In keeping with our previous analysis of Lhx6 and Foxp2 (Hernandez et al., 2015), we observed no overlap between Nkx2.1$^+$ neurons and Foxp2-expressing (Foxp2$^+$) neurons in wild-type brain sections (*n* = 1 out of 1,131 Nkx2.1$^+$ neurons, 3 sections; *n* = 1 out of 414 Foxp2$^+$ neurons, 3 sections). To effectively determine how Nkx2.1 intersects with the remaining GPe neuron types, we made a Nkx2.1-F-tdTom (Nkx2.1-Flp;FSF-tdTomato) genetic cross, which yielded robust tdTomato labeling (tdTomato$^+$) in the GPe. In addition to tdTomato$^+$ neurons, we observed tdTomato$^+$ glia in the GPe that were distinguished from neurons based on their morphology. To assess the legacy recombination events in Nkx2.1-F-tdTom, we compared tdTomato expression to Nkx2.1 immunolabeling. Immunoreactivity on Nkx2.1-F-tdTom brain sections with tdTomato, Nkx2.1, and HuCD antibodies revealed ~90% (89 ± 8%, *n* = 809 neurons, 3 sections) of tdTomato$^+$ neurons colocalizing with Nkx2.1$^+$ neurons (**Figure 1**). While we observed significant tdTomato$^+$ labeling throughout the entire cortex, Nkx2.1 immunoreactivity was absent. These data corroborate previous findings that Nkx2.1 is downregulated in cortical interneurons (Butt et al., 2008) and argue that GPe neurons maintain Nkx2.1 expression into adulthood. Similarly, we observed no cell bodies in the TRN (**Figure 1**), STN, and SNr that were Nkx2.1$^+$ (not shown). Subsequent immunohistological analysis of Nkx2.1 expression with established GPe markers revealed that the majority of Nkx2.1$^+$ neurons are PV$^+$ (71 ± 3%, *n* = 1105 neurons, 7 sections), while there is a smaller subset that are Npas1$^+$ (17 ± 2%, *n* = 383 neurons, 6 sections) or Lhx6$^+$ (41 ± 7%, *n* = 1,469 neurons, 9 sections) (**Table 3**). It is important to note that Nkx2.1$^+$ neurons are only ~80% (83 ± 4%, *n* =

1105 neurons, 7 sections) of PV$^+$ neurons. These findings are consistent with previous observations (Xu et al., 2008). Furthermore, Nkx2.1$^+$ neurons represent ~80% (78 ± 8%, n = 1469 neurons, 9 sections) of Lhx6$^+$ neurons and only a subset of Npas1$^+$ neurons (32 ± 1%, *n* = 383 neurons, 6 sections). More importantly, nearly all Npas1$^+$-Nkx2.1$^+$ neurons are Lhx6$^+$ (90 ± 5%, *n* = 184 out of 204 neurons, 3 sections). Accordingly, the Npas1$^+$-Nkx2.1$^+$ and Npas1$^+$-Lhx6$^+$ populations of Npas1$^+$ neurons are nearly identical (33 ± 5%, *n* = 204 out of 609 neurons, 3 sections and 32 ± 3%, *n* = 233 out of 609 neurons, 3 sections, respectively).

Sox6 delineates GPe neuron subtypes

Previous literature demonstrates that Sox6 is present in most, if not all, medial ganglionic eminence (MGE) derived neurons in the mature brain (Azim et al., 2009; Batista-Brito et al., 2009). Moreover, Sox6 and Lhx6 are extensively colocalized within the MGE (Batista-Brito et al., 2009). This corroborates the idea that Sox6 is a downstream signaling partner of Lhx6 (Azim et al., 2009; Batista-Brito et al., 2009). In view of these findings, we set out to examine the Sox6 expression pattern in the GPe. Sox6 immunolabeling revealed ~65% (64 ± 4%, *n* = 4,681 neurons, 14 sections) of GPe neurons express this transcription factor. To determine the relationship between Sox6-expressing (Sox6$^+$) and Nkx2.1, we first investigated Sox6 expression in Nkx2.1$^+$ neurons. By examining Nkx2.1-F-tdTom brain sections, we found substantial overlap between tdTomato$^+$ neurons and Sox6$^+$ neurons (68 ± 1% out of Nkx2.1, *n* = 681 neurons, 3 sections; 58 ± 0% out of Sox6, *n* = 681 neurons, 3 sections) (**Table 3**). Although both Sox6 and Nkx2.1 are expressed in ~60–65% of GPe neurons, they do not represent the same pool of neurons as they have distinct contributions to GPe subtypes (**Table 3**). A close examination of Sox6$^+$ neurons revealed that nearly all Npas1$^+$ neurons are Sox6$^+$ (93 ± 6%, *n* = 1,999 neurons, 14 sections), while only half of the PV$^+$ population expresses Sox6 (53 ± 8%, *n* = 1,675 neurons, 15 sections). In contrast, Nkx2.1$^+$ neurons account for ~32% of Npas1$^+$ neurons and ~83% of PV$^+$ neurons.

Next, we examined the relationship between the Sox6 and Lhx6 GPe neuron populations as this may yield important insights into whether we can target the otherwise inaccessible Lhx6$^+$-PV$^-$-Npas1$^-$ population. As no specific antibody for Lhx6 is available, we use the GFP expression in Lhx6-GFP mice as a proxy for Lhx6

expression. Overall, Lhx6$^+$ GPe neurons represent a third of GPe neurons (34 ± 8%, *n* = 2,533 neurons, 12 sections) and are made up of approximately 30% PV$^+$ neurons (28 ± 7%, *n* = 654 neurons, 12 sections), 35% Npas1$^+$ neurons (35 ± 5%, *n* = 818 neurons, 12 sections), and 7% ChAT$^+$ neurons (7 ± 1%, *n* = 48 neurons, 3 sections). To determine the relationship between Sox6 expression within the Lhx6$^+$, PV$^+$, and Npas1$^+$ populations, immunolabeling on Lhx6-GFP sections showed that Sox6 was expressed in ~75% (76 ± 7%, n = 2346 neurons, 15 sections) of Lhx6$^+$ neurons as well as all PV$^+$ neurons and Npas1$^+$ neurons that were Lhx6$^+$ (**Figure 2**). Consistent with our previous observations (Hernandez et al., 2015), we observed negligible overlap between Lhx6$^+$ and Foxp2$^+$ GPe neurons (8 out of 1,882 neurons, 3 sections).

Taken together, our data reveal a Lhx6$^+$ population (51 ± 6%, *n* = 229 out of 455 neurons, 3 sections) that is devoid of both PV and Npas1 expression. A portion of this Lhx6$^+$-PV$^-$-Npas1$^-$ population is Sox6$^-$ (24 ± 6%, *n* = 938 neurons, 15 sections) and represents 11% of all GPe neurons. Furthermore, a small population (15%) of Lhx6$^+$ neurons exists that expresses Sox6, but not PV or Npas1, and this accounts for ~5% of the entire GPe. Given that 7% of Lhx6$^+$ neurons express ChAT, and we observed no overlap between ChAT and Sox6 (0 out of 1,674 neurons, 3 sections), we were able to pinpoint the molecular identity of ~97% of Lhx6$^+$ neurons. While Sox6 and Nkx2.1 differ in their relative overlap with GPe markers, it is important to note that the Lhx6$^+$-Nkx2.1$^+$ population is likely equivalent to the Lhx6$^+$-Sox6$^+$ population. We found both Nkx2.1 and Sox6 overlap similarly with Lhx6$^+$ (Nkx2.1 out of Lhx6, 78 ± 8%, *n* = 1,469 neurons, 9 sections; Sox6 out of Lhx6, 76 ± 7%, *n* = 2,346 neurons, 15 sections), and the Lhx6$^+$-Nkx2.1$^+$ and Lhx6$^+$-Sox6$^+$ populations are similarly abundant within the entire GPe (28 ± 7% and 32 ± 6%, respectively). It is therefore possible that this Lhx6$^+$-Sox6$^+$ population is also Nkx2.1$^+$. However, with our present tools, we cannot confirm the assertion that these two subtypes are identical.

Dbx1-L-tdTom mice label a heterogenous GPe neuron subset

Though Lhx6$^+$-Sox6$^-$ neurons constitute a substantial fraction (11%) of the GPe, we do not have direct access to this population. Neurons from the Dbx1 lineage originate from the preoptic area (PoA) and are known to populate the GPe (Nobrega-Pereira et al., 2010). Considering Lhx6 is expressed in postmitotic neurons derived from both

the MGE and the PoA (Du et al., 2008; Fogarty et al., 2007), we set out to investigate if neurons from the Dbx1 lineage correspond to Lhx6^{+}-Sox6^{-} GPe neurons. Accordingly, we identified neurons that arise from the Dbx1 lineage and determined their relationship with the Lhx6^{+}-Sox6^{-} GPe subset by using a Dbx1-L-tdTom (Dbx1-Cre;LSL-tdTomato) cross, which produced robust tdTomato expression in the GPe. Immunolabeling with HuCD and tdTomato confirmed the neuronal nature of tdTomato-labeled cells (**Figure 2**). These neurons account for ~9% of the entire GPe population (9 ± 1%, *n* = 2,593 neurons, 52 sections). In addition to neuronal labeling, tdTomato^{+} glia were present within the GPe and densely populated the ventral GPe border. For simplicity, we refer to tdTomato^{+} neurons in Dbx1-L-tdTom mice as Dbx1^{+} neurons. Immunohistological analysis of Dbx1^{+} neurons showed substantial co-expression with Nkx2.1 (78 ± 10%, *n* = 329 neurons, 9 sections) and Sox6 (52 ± 8%, *n* = 442 neurons, 15 sections). Furthermore, Dbx1^{+} neurons are primarily PV^{+} (72 ± 8% *n* = 493 neurons, 23 sections) and to a lesser extent Npas1^{+} (10 ± 5% *n* = 72 neurons, 14 sections), ChAT^{+} (7 ± 3% *n* = 34 neurons, 9 sections), and Foxp2^{+} (4 ± 2% *n* = 13 neurons, 10 sections). To summarize, we found Dbx1^{+} neurons do not correspond to the Lhx6^{+}-Sox6^{-} unique GPe subset. Despite both populations representing ~10% of GPe neurons, they vary in their co-expression of PV, Npas1, and Sox6. Coexpression of Lhx6 in Dbx1^{+} neurons was not examined in this study for technical reasons; however, due to the close functional relationship between Nkx2.1, Sox6, and Lhx6, it can be inferred that Lhx6 represents a substantial fraction of Dbx1^{+} neurons.

Dbx1^{+}-PV^{+} neurons exhibit canonical PV^{+} neurons projection patterns

Although Dbx1^{+} neurons only account for ~10% of GPe neurons, it is possible that they target a unique area and serve an important function. As Cre is not expressed in adult Dbx1-Cre mice (Bielle et al., 2005), we do not have true genetic access to this neuron population. Rather than relying on standard Cre-inducible viral approaches, Alexa-conjugated cholera toxin b (CTb), a widely-used retrograde tracer, was used to map the axonal projection patterns of Dbx1^{+} neurons. Given the majority of Dbx1^{+} neurons are PV^{+}, we first targeted the STN, the principal recipient of PV^{+} GPe input, in our connectome survey (Hegeman et al., 2016; Hernandez et al., 2015). As expected, we found Dbx1^{+} neurons project primarily to the STN (23 ± 9%, *n* = 94 neurons, 9 sections) (**Figure 3**, **Table 4**).

Additionally, but to a much lesser extent, we found Dbx1$^+$ neurons project to the substantia nigra pars reticulata (SNr, 2 ± 0%, *n* = 20 neurons, 9 sections). These numbers are likely an underestimation due to incomplete coverage of the target areas (i.e. STN and SNr) with these injections. Importantly, although ~10% of Dbx1$^+$ GPe neurons co-express Npas1, we observed no projections to the dorsal striatum (0 out of 42 CTb$^+$ neurons) (**Table 4**). The negative results were not due to poor labeling efficiency as neighboring Dbx1$^-$ neurons were evidently labeled in the same section. To examine if Dbx1$^+$ neurons account for the recently described non-cholinergic, cortically-projecting GPe neurons (Ahrlund-Richter et al., 2019; Chen et al., 2015; Saunders et al., 2015; Schwarz et al., 2015), CTb was injected into various cortical regions of Dbx1-L-tdTom mice. Systemic analysis of multiple cortical areas including the somatomotor (MO, *n* = 4 mice), somatosensory (SS, *n* = 2 mice), anterior cingulate (AC, *n* = 1 mouse), agranular (AG) and orbital (ORB, *n* = 2 mice) cortices revealed Dbx1$^+$ neurons do not project to any of these cortical regions (0 out of 52 neurons, 9 sections). These were not just failed injections, as there were CTb$^+$ neurons within the GPe (see below).

To confirm that the findings from retrograde tracing were not just due to obscure biases with the CTb, a pseudotyped-lentivirus was used for retrograde delivery of Cre recombinase (LVretro-Cre) (Knowland et al., 2017). Unlike CTb, this strategy gives more robust, unambiguous cytoplasmic tdTomato expression. CTb and LVretro-Cre were injected into various known areas that receive GPe input, including dSr, STN, SNr, parafascicular nucleus (PF) (Kita, 2007). We observed comparable labeling patterns with LVretro-Cre and CTb injections into the dStr (Npas1$^+_{\text{LVretro}}$: 75 ± 8%, *n* = 200 out of 277 neurons; Npas1$^+_{\text{CTb}}$: 100 ± 0%, *n* = 18 out of 23 neurons) and STN (PV$^+_{\text{LVretro}}$: 76 ± 7%, *n* = 278 out of 377 neurons; PV$^+_{\text{CTb}}$: 73 ± 11%, *n* = 263 out of 425 neurons). A different scenario was observed with SNr injections—there was not a predominant neuron class that projected to the SNr (PV$^+_{\text{LVretro}}$: 67 ± 26%, *n* = 51 out of 69 neurons; PV$^+_{\text{CTb}}$: 35 ± 12%, *n* = 22 out of 108 neurons) (**Figure 3**, **Table 4**). The relatively low cell-specificity and discrepancies between LVretro-Cre and CTb observed in the SNr data could be the result of a number of factors including complex topographical organization of the GPe projection and CTb spreading into areas that are adjacent to the SNr that receive Npas1$^+$ input (e.g., substantia nigra pars compacta). Furthermore, LVretro-Cre and CTb injections into the PF yielded labeling throughout the cortex, most prominently

in the MOs, MOp, and agranular regions (**Figure 3**), consistent with prior observations (Mandelbaum et al., 2019; Sherman, 2016). However, contrary to reports of a GPe-PF connection from other laboratories (Mastro et al., 2014), we observed no labeling in the GPe with these injections (LVretro-Cre, 4 mice; CTb, 9 mice). It is possible that CTb and LVretro-Cre both have low labeling efficiencies, making it difficult to conclude the absence of sparse projections.

Npas1$^+$-Nkx2.1$^+$ neurons are part of the cortico-GPe-cortical loop

While we found no Dbx1$^+$ neurons projecting to the cortex, we identified a subset of GPe neurons that are cortex-projecting. CTb-based tracing revealed primary somatosensory (SSp, aka S1), primary somatomotor (MOp, aka M1), AG and ORB cortices as the primary targets of cortical-projecting GPe neurons (CTb, n = 116 neurons, 21 sections). To confirm these regions as the primary targets, we injected LVretro-Cre into frontal cortical regions of LSL-tdTomato mice. Unlike CTb, this strategy gives more robust, unambiguous cytoplasmic tdTomato expression. We observed a population of retrogradely labeled GPe neurons, i.e. tdTomato$^+$ (LV, n = 286 neurons, 27 sections) (**Figure 4**).

Though cortical input is known to reach the GPe through the cortico-dStr-GPe and the cortico-STN-GPe pathways (Jaeger and Kita, 2011), there is increasing evidence of direct cortical input to the GPe (Milardi et al., 2015; Naito & Kita, 1994; Smith & Wichmann, 2015). Using rabies virus tracing, we have recently confirmed the existence of cortical input to GPe neurons (Hunt et al., 2018). However, with the low density mapping and manual quantification, we were not able to provide a more complete representation of the input regions and their relative size. In this study, we sought to map the input from the entire cortical mantle with LVretro-Cre in LSL-tdTomato mice. Automated, serial two-photon tomography was used to provide an unbiased quantification and atlas registration (see Materials and Methods). As expected, input neurons (i.e. tdTomato$^+$) from a wide array of brain regions to the GPe were evident (data not shown). A full description of the brain-wide input to the GPe will be detailed in a later publication. The cortical input to the GPe amounts to ~10% of the total input (n = 4,205 out of 45,223 neurons, 8 mice). Consistent with our previous observation, a notable input comes from the SSp followed

by MOp. Additionally, but to a much lesser extent, input cells were found in MOs, SSs, and lateral regions, such as gustatory area, visceral area, and claustrum. These results are summarized in **Figure 4**.

A substantial amount of these cortex-projecting neurons displayed a distinctive larger soma and were located in the caudoventral regions of the GPe—features that are characteristic of ChAT$^+$ neurons (**Figure 4**). Immunolabeling for ChAT revealed 50% (50 ± 0%, *n* = 19 out of 42 neurons, 3 sections) of tdTomato$^+$ neurons were ChAT$^+$. The remaining cortex-projecting GPe neurons were ChAT$^-$, i.e., non-cholinergic. Our results are highly consistent with prior observations (Ahrlund-Richter et al., 2019; Saunders et al., 2015). However, as the identity of non-cholinergic, cortically-projecting neurons remains elusive, we sought to characterize the molecular profile of these neurons. Through immunolabeling for ChAT and Nkx2.1, we identified the ChAT$^-$ neurons to be Nkx2.1$^+$ (32 ± 6%, *n* = 20 out of 68 neurons, 6 sections) and Npas1$^+$ (25 ± 6%, *n* = 41 out of 147 neurons, 13 sections). Furthermore, immunolabeling confirmed a population of cortex-projecting neurons that was both Nkx2.1$^+$ and Npas1$^+$ (20 ± 7%, *n* = 8 out of 36 neurons, 3 sections) (**Table 4**). As expected, the same neurons that expressed Npas1 and Nkx2.1 did not express Foxp2 (0 out of 36 neurons, 3 sections) (**Figure 5**). Similarly, we observed a very small fraction of neurons that were immuno-positive for PV (0 ± 0%, *n* = 3 out of 65 neurons, 8 sections). While abundant retrogradely-labeled neurons were found with injections targeting MOp, SSp, agranular and orbital cortices, we observed low levels or non-detectable retrograde labeling with injection to neighboring frontal regions such as secondary somatomotor (MOs, aka M2) and secondary somatosensory (SSs, aka S2) cortices.

Npas1$^+$ GPe neurons form functional connections within the cortex

To further demonstrate that Npas1$^+$ neurons project to the cortex, we injected Npas1-Cre mice with a Cre-inducible ChR2-eYFP AAV (see Materials and Methods) into the GPe to trace the arborization patterns of Npas1$^+$ axons. Consistent with our previous studies (Glajch et al., 2016; Hernandez et al., 2015), dense Npas1$^+$ axons were visible in the dStr. Moreover, we observed axons throughout the MO and SS, but its density dropped off precipitously once passed the ORB. These axons appeared to arborize heavily in layers 5 and 6 and were present as superficial as layer 2/3 (**Figure 4**). Under high-magnification, perisomatic basket-like structures can be found

in layer 5 of the MO. In addition, Npas1$^+$ axons were found in the TRN with more moderate projections in the zona incerta (ZI) and SN. Within the SN, we observed a higher density of fibers in the SNc than the SNr (not shown). The presence of Npas1$^+$ axons in the TRN is consistent with the high density of Nkx2.1$^+$ synaptic boutons in the area (**Figure 5**). As TRN neurons do not express Nkx2.1, the synaptic boutons observed arose from an extrinsic source. Our observations further suggest the molecular identity of GPe neurons that form this projection and is consistent with previously tracing data that demonstrate an anatomical connection from the GPe to the TRN (Asanuma, 1989, 1994; Clemente-Perez et al., 2017; Cornwall et al., 1990; Gandia et al., 1993; Hazrati and Parent, 1991; Kayahara and Nakano, 1998; Pazo et al., 2013; Shammah-Lagnado et al., 1996).

Anatomical data suggest synaptic connections are made by Npas1$^+$-Nkx2.1$^+$ neurons, specifically in the cortex and TRN. However, contact probability and the physiological properties of the synaptic connections cannot be inferred from the anatomical data. To this end, optogenetic-based mapping and patch-clamp recordings were performed. As Npas1 axons target primarily cortical layers 5 and 6, neurons in those layers were targeted for recording. In 3 out of 37 neurons recorded, large (438.5–821.7 pA, n = 3 neurons) inhibitory postsynaptic currents (IPSCs) were evoked by optogenetic activation of Npas1$^+$ axons from the GPe (see Materials and Methods). These were not conducting events, as they were not abolished by the co-application of tetrodotoxin (1 μM) and 4-aminopyridine (100 μM). To confirm the GABAergic nature of the events, SR95531 (a $GABA_A$ receptor antagonist, 10 μM) was applied, which completely abolished evoked IPSCs (**Figure 5**). In contrast to the apparent low connection probability in the cortex, large IPSCs were readily evoked optogenetically in all but one of the TRN neurons tested (707.8 ± 383.8 pA, n = 5 neurons). Importantly, as identical optogenetic conditions were used for both experiments, these data argue that the low connection probability detected in the cortex is reflecting a selective targeting of cortical neuron subtypes by Npas1$^+$ axons. No photocurrents were observed in any of the recorded neurons, ruling out potential contributions of the synaptic events from ectopic infection of neurons local to the recorded areas.

To confirm axons observed in the frontal cortex were not a result of ectopic infection of caudal cortical regions, we injected the same Cre-inducible ChR2-eYFP AAV into the SSp region directly above the GPe. We

observed only sparse cortico-cortical axons running rostrocaudally (**Figure 4**), further confirming that the axons observed in the frontal regions were indeed projections from Npas1$^+$ GPe neurons.

Lhx6$^+$ neuron subtypes have unique spatial patterns

Spatial distribution may vary with neuronal identity as seen in the cortex, for example, where neurons are organized in a highly laminar-specific manner (Harris and Shepherd, 2015; Huang et al., 2007; Wamsley and Fishell, 2017). We therefore integrated spatial distribution as a metric to phenotype different GPe neuron types (**Figure 7**). Overall, more neurons populate towards the rostral pole of the GPe. We noted that ChAT neurons and Lhx6$^+$-Sox6$^+$ neurons are displaced more heavily toward the caudoventral regions and rostroventral regions, respectively. All other identified neurons are distributed throughout the GPe. This analysis, however, does not capture any lateromedial gradients. As neurons were routinely sampled across three different lateromedial planes across the GPe, the abundance of identified neurons were tallied. Consistent with previous studies (Hernandez et al., 2015; Mastro et al., 2014), we observed a lateromedial gradient in PV$^+$ neurons (lateral = 46 ± 10%, *n* = 4,368 neurons, 24 sections; intermediate = 45 ± 11%, *n* = 5,113 neurons, 27 sections; medial = 32 ± 7%, *n* = 2,829 neurons, 20 sections) and Lhx6$^+$ neurons (lateral = 28 ± 6%, *n* = 1,422 neurons, 10 sections; intermediate = 42 ± 9%, *n* = 2,050 neurons, 10 sections; medial = 45 ± 12%, *n* = 2,190 neurons, 8 sections). PV$^+$ neurons were more concentrated in the lateral than the medial level; the reverse pattern is found for Lhx6$^+$ neurons. In **Figure 6**, we illustrate the distribution of Lhx6$^+$-Sox6$^-$ neurons (lateral = 8 ± 4%, *n* = 187 neurons, 5 sections; intermediate = 10 ± 1%, *n* = 292 neurons, 5 sections; medial = 21 ± 7%, *n* = 459 neurons, 5 sections), which follow the same pattern as pan-Lhx6$^+$ neurons. While PV$^+$-Lhx6$^+$ neurons displayed a similar pattern (lateral = 8 ± 2%, *n* = 116 neurons, 4 sections; intermediate = 11 ± 6%, n = 202 neurons, 3 sections; medial = 8 ± 1%, *n* = 175 neurons, 3 sections) as pan-Lhx6$^+$ neurons, Npas1$^+$-Lhx6$^+$ neurons do not (lateral = 14 ± 3%, *n* = 231 neurons, 4 sections; intermediate = 15 ± 2%, *n* = 308 neurons, 4 sections; medial = 14 ± 2%, *n* = 284 neurons, 4 sections). The lateromedial gradient of different GPe neuron types are summarized in **Figure 6**.

GPe neuron subtypes have distinct intrinsic properties

To further define GPe neuron subtypes, *ex vivo* electrophysiological analyses were performed systematically on a number of genetically-identified GPe neuron subtypes. The focus of these experiments was to compare the less well-studied neuron subtypes. We used recording and analysis routines (see Materials and Methods) identical to those used in our previous study to facilitate cross-comparison between the two (Hernandez et al., 2015).

To identify Foxp2$^+$ neurons, we infected Foxp2-Cre mice with a CreOn-mCherry AAV (see Materials and Methods). To confirm the validity of the approach, a subset of these mice were examined for cellular specificity of Cre-mediated mCherry expression (mCherry$^+$). In nearly all mCherry$^+$ neurons examined, Foxp2 was expressed (100 ± 0%, n = 473 out of 485 neurons, 6 sections) (**Figure 8**). No GPe neurons expressed mCherry when the same virus was injected in wild-type mice (n = 2 mice, 6 sections). During the course of our study, we noted that Lhx6$^+$ neurons can be categorized into "bright" and "dim" based on their GFP expression level. The definitive identities of Lhx6$^+_{bright}$ and Lhx6$^+_{dim}$ were not confirmed *post hoc*. We refrain ourselves from over-interpreting the results. To identify PV$^+$-Dbx1$^+$ neurons, an intersectional cross was made—PV-Dbx1-FL-tdTom (PV-Flp;Dbx1-Cre;LSL-FSF-tdTomato) to label PV$^+$-Dbx1$^+$ neurons (tdTomato$^+$). To unequivocally identify Npas1$^+$-Lhx6$^+$ neurons, which are equivalent to Npas1$^+$-Nkx2.1$^+$ neurons, we crossed Npas1-tdTom and Lhx6-GFP mice. Double-positive (tdTomato$^+$ and GFP$^+$) neurons were targeted for recordings. ChAT$^+$ neurons, which can be identified based on their unique somatodendritic morphology, were not included in this analysis as we have previously established that they have a very distinct electrophysiological profile (Hernandez et al., 2015). Lastly, because we do not have genetic access to Lhx6$^+$-Sox6$^-$ neurons, we did not have means to target them for direct recording.

To highlight, Foxp2$^+$ neurons and PV$^+$-Dbx1$^+$ neurons were at the extremes in terms of their spontaneous activity measured in cell-attached recordings (Foxp2$^+$ = 6.07 ± 1.91 Hz, n = 20; PV$^+$-Dbx1$^+$ = 18.42 ± 2 Hz, n = 16), with the rest of the neuron subtypes displaying properties traversing the spectrum. Furthermore, our results corroborate findings from our prior studies (Hernandez et al., 2015) that PV$^+$ neurons fire at a higher rate than Npas1$^+$ neurons (PV$^+$ = 16.7 ± 3 Hz, n = 111; Npas1$^+$ = 8.13 ± 3.26 Hz, n = 67, P < 0.0001). Lhx6$^+$ neurons exhibited firing rates that are in between PV$^+$ neurons and Npas1$^+$ neurons (Lhx6$^+$ = 10.6 ± 5.12 Hz, n = 42). Within the Lhx6$^+$

560 population, Lhx6$^{+}_{bright}$ neurons and Lhx6$^{+}_{dim}$ neurons exhibited different firing rates (Lhx6$^{+}_{bright}$= 9.5 ± 1.71 Hz, *n* = 16; Lhx6$^{+}_{dim}$= 16.5 ± 1.2 Hz, *n* = 7, *P* = 0.0076). Additionally, the Npas1^{+}-Lhx6^{+} neurons had a higher spontaneous firing than the Foxp2^{+} population (Npas1^{+}-Lhx6^{+} = 10.4 ± 2.8 Hz, *n* = 14, *P* = 0.0026) but was comparable to Lhx6$^{+}_{bright}$ neurons (*P* = 0.3391) **Figure 8**. As expected, Dbx1^{+} neurons exhibited firing behavior that was most consistent with its composition, with most neurons exhibiting similar firing rates to PV^{+} neurons and some more 565 similar to Npas1^{+} neurons (See **Table 5** and **6**, Dbx1^{+} = 13.2 ± 4 Hz, *n* = 21).

As we have previously shown that the regularity of the firing varied with GPe neuron types (Hernandez et al., 2015), we measured the coefficient of variation (CV) in the interspike-interval. Consistent with our prior observations, PV^{+} neurons exhibited a lower CV than Npas1^{+} neurons (PV^{+} = 0.14 ± 0.04, *n* = 87; Npas1^{+} = 0.28 ± 0.09, *n* = 62, *P* < 0.0001). Dbx1^{+} neurons and PV^{+}-Dbx1^{+} neurons had CVs that are statistically similar to PV^{+} 570 neurons (Dbx1^{+} = 0.14 ± 0.02, *n* = 20; PV^{+}-Dbx1^{+} = 0.16 ± 0.05, *n* = 16). Foxp2^{+} neurons had the largest variability in their firing rate, and accordingly, the highest CV within the GPe neuronal population (Foxp2^{+} = 0.36 ± 0.10, *n* = 20). Npas1^{+}-Lhx6^{+} neurons had CV statistically similar to the Lhx6$^{+}_{bright}$ neurons (Npas1^{+}-Lhx6^{+} = 0.25 ± 0.07 *n* = 14, Lhx6$^{+}_{bright}$ = 0.20 ± 0.04, *n* = 16, *P* = 0.3338) and different from the Foxp2^{+} neurons (*n* = 20, *P* = 0.0204).

To provide comprehensive electrophysiological profiles, we investigated a range of electrophysiological 575 properties of GPe neurons in whole-cell current-clamp recordings. As seen in prior studies, PV^{+} neurons had the highest maximum firing rate (PV^{+} = 192 ± 20 Hz, *n* = 26). Lower maximum firing rates were observed in Npas1^{+} neurons and Foxp2^{+} neurons (Npas1^{+} = 94 ± 34 Hz, *n* = 32; Foxp2^{+} = 55 ± 23, *n* = 16) when compared to PV^{+}, Dbx1^{+}, and PV^{+}-Dbx1^{+} neurons (*P* < 0.0001 for all*).* Within Lhx6, Lhx6$^{+}_{bright}$ neurons and Lhx6$^{+}_{dim}$ neurons exhibited different maximum firing rates (Lhx6$^{+}_{bright}$= 102 ± 32 Hz, *n* = 21; Lhx6$^{+}_{dim}$= 162 ± 9 Hz, *n* = 7, *P* < 0.0001). GPe 580 neuron subtypes also exhibited different responses to hyperpolarizing current injections. More negative trough potentials were noted in the Npas1^{+} neurons and Foxp2^{+} neurons (Npas1^{+} = −146.6 ± 16.6 mV, *n* = 44; Foxp2^{+} = −166.1 ± 7.57 mV, *n* = 16) when compared to PV^{+} neurons (*P* < 0.0001 for both). Within Lhx6^{+} neurons, Lhx6$^{+}_{bright}$ neurons and Lhx6$^{+}_{dim}$ exhibited different trough potentials (Lhx6$^{+}_{bright}$= −132.5 ± 12.3 mV, *n* = 21, Lhx6$^{+}_{dim}$= −111.3 ± 10.5 mV, *n* = 9, *P* = 0.0113). The trough potential observed in Npas1^{+}-Lhx6^{+} neurons (Npas1^{+}-Lhx6^{+} = −118.5 ±

10.5 mV, *n* = 16) was less negative than either Npas1$^+$ neurons (*P* = 0.0031) or Foxp2$^+$ neurons (*P* = 0.0012). As seen in previous work from our lab (Hernandez et al., 2015), PV$^+$ and PV$^+$-Dbx1$^+$ neurons exhibited the least negative trough potential compared to the other studied GPe neuron types and were not different from one another (*P* = 0.1078) (PV$^+$ = −95.1 ± 6.3 mV, *n* = 51, PV$^+$-Dbx1$^+$ = −88.4 ± 16.3 mV, *n* = 21). Dbx1$^+$ neurons had trough potential (Dbx1$^+$ = −104.3 ± 8.6 mV, n = 24) more negative than those seen in PV$^+$ neurons (P = 0.0008) and PV$^+$-Dbx1$^+$ neurons (P = 0.0020) . Similar to the trough potentials, higher Sag ratios were observed for Npas1$^+$ neurons and Foxp2$^+$ neurons (Npas1$^+$ = 1.24 ± 0.14, *n* = 44; Foxp2$^+$ = 1.33 ± 0.13, *n* = 16). PV$^+$ neurons had the lowest sag ratio (PV$^+$ = 1.10 ± 0.03, *n* = 18). Within Lhx6, a difference in the Sag ratio was observed between Lhx6$^+_{bright}$ neurons and Lhx6$^+_{dim}$ neurons (Lhx6$^+_{bright}$= 1.21 ± 0.09, *n* = 21, Lhx6$^+_{dim}$= 1.14 ± 0.04, *n* = 9, *P* = 0.0279). The Npas1$^+$-Lhx6$^+$ neurons exhibited a lower sag ratio than both Npas1$^+$ neurons (Npas1$^+$-Lhx6$^+$ = 1.06 ± 0.04, *n* = 16, *P* = 0.0024) or Foxp2$^+$ neurons (*P* < 0.0001). As expected, the PV$^+$-Dbx1$^+$ neurons and Dbx1$^+$ neurons had statistically similar sag ratios as the PV$^+$ neuron population (Dbx1$^+$ = 1.14 ± 0.07, *n* = 24; PV$^+$-Dbx1$^+$ = 1.13 ± 0.08, *n* = 21).

In summary, Npas1$^+$-Lhx6$^+$ neurons have intrinsic properties that are comparable with Lhx6$^+_{bright}$ neurons but are distinct from Foxp2$^+$ neurons. Furthermore, Dbx1$^+$-PV$^+$ neurons exhibit canonical PV$^+$ neuron intrinsic properties. Overall, these data corroborate and extend our previous findings. A full description of the different electrophysiological parameters and pairwise statistical comparisons across the different neuron subtypes are listed in **Table 5** and **6**.

Discussion (1699 words)

In this study, we used novel transgenic mice, immunolabeling, electrophysiology, and circuit analyses to generate a more comprehensive landscape of GPe neuron composition. Specifically, we provided a more complete investigation of the Lhx6$^+$ and Dbx1$^+$ populations, along with novel insight into the properties of neurons arising from the Sox6 lineage. Our current study further illustrates the complexity of GPe neurons in adult mice and infers the existence of possible, new neuron subclasses. In particular, our results support the idea that Npas1$^+$-Nkx2.1$^+$ neurons are a distinct GPe neuron subclass.

Toward a more complete description of the GPe

We hypothesized the existence of a unique population of Lhx6$^+$ neurons in the GPe accounting for at least 15% of the GPe. This idea is supported by our own data, along with others (Dodson et al., 2015; Hegeman et al., 2016; Hernandez et al., 2015; Mastro et al., 2014). In this study, we first set out to examine the expression of Nkx2.1, Lhx6, and Sox6 among GPe neurons, as these transcription factors dictate cell fates. The examination of Sox6 expression unequivocally confirmed the existence of this unique Lhx6$^+$ population—however, to our surprise, this unique Lhx6$^+$ population is Sox6$^-$. As Sox6 is described as MGE-enriched, one would expect its expression in all Lhx6$^+$ neurons. This finding was unexpected. Importantly, our results resolve some of the discrepancies related to Lhx6$^+$ neurons and identify the PV$^-$ and Npas1$^-$ neurons described in our previous study (Hernandez et al., 2015).

While Dbx1$^+$ neurons that originate from the PoA are known to populate the GPe (Gelman et al., 2009; Nobrega-Pereira et al., 2010), their properties are not well-characterized. We examined whether Dbx1$^+$ neurons correspond to the Lhx6$^+$-Sox6$^-$ population. Contrary to our hypothesis, our data argue that Dbx1$^+$ neurons do not at all correspond to this population of neurons. Instead, we found the Dbx1$^+$ population contains neurons that express, to varying degrees, all established GPe neuron markers (**Figure 2, Table 3**). This is consistent with the literature that PoA progenitors give rise to a small, but diverse, contingent set of neurons (Gelman et al., 2011; Gelman et al., 2009). In particular, most Dbx1$^+$ neurons are Sox6$^+$, and they primarily express PV$^+$ or Npas1$^+$. In

hindsight, these results were not completely unexpected. While the embryonic PoA is similar to the MGE in that it expresses the transcription factor Nkx2.1, many PoA cells do not express Lhx6 (Flames et al., 2007). It has been shown that a subset of LGE (lateral ganglionic eminence) progenitors express Lhx6 (Liodis et al., 2007). Importantly, the LGE is known to generate GABAergic neurons that populate the cortex (Anderson et al., 2001; de Carlos et al., 1996; Jimenez et al., 2002; Tamamaki et al., 1997). Therefore, it is possible that this Lhx6^{+}-Sox6^{-} GPe population arises from the LGE. Alternatively, the GFP expression in the Lhx6^{+}-Sox6^{-} neurons can also be completely ectopic. Unfortunately, as we do not have direct genetic access to this population, it was not feasible to target them for further analyses. We await new tools that give us unique access to the Lhx6^{+}-Sox6^{-} population. Nonetheless, the Sox6-Cre line is available and will allow us to assess other neuron subtypes (see below). On the other hand, it is interesting to see that PV^{+}-Dbx1^{+} neurons display a phenotype that is shared with the general PV^{+} population, which originate primarily from the MGE (Flandin et al., 2010; Nobrega-Pereira et al., 2010). Although the extent of the overlap remains to be fully established, our findings are in line with what was shown previously that neurons that arise from spatially-distinct ontogenic domains converge onto a single neuron class (Chittajallu et al., 2013). However, it is intriguing to hypothesize that brain states, imposed by yet to be identified neuromodulatory signals, may have differential impacts on these neuron subtypes. High-throughput single-cell transcriptomic analysis has become an extremely powerful tool for cell classification. However, as both Lhx6^{+}-Sox6^{-} and Dbx1^{+} neurons are rather sparse in the GPe, they are likely underrepresented in previous single-cell transcriptomic studies (Saunders et al., 2018; Zeisel et al., 2018). Our current study has thus provided important insight into these low abundance neurons.

Though our connectome survey did not reveal either Lhx6^{+}-Sox6^{-} neurons or Dbx1^{+} neurons to be cortically-projecting, it pinpointed Npas1^{+}-Nkx2.1^{+} neurons as key constituents of the cortico-GPe-cortical loop. Our motivation to investigate the Nkx2.1-Lhx6-Sox6 lineage was a logical step, but our findings with Npas1^{+}-Nkx2.1^{+} neurons are completely serendipitous. In summary, our findings revealed that Npas1^{+}-Nkx2.1^{+} neurons are distinct from Npas1^{+}-Foxp2^{+} neurons. Accordingly, both of them should be regarded as *bona fide* subclasses. Moreover, we show that Nkx2.1 and Foxp2 only make up ~90% of the entire Npas1 population; this suggests a

potential third subtype of Npas1$^+$ neurons. Our data hinted at the diversity of PV$^+$ neurons. Yet, we do not have sufficient data to argue if they fall into different neuron subclasses. Based on enhancer/transgenic mice, Silberberg and colleagues (Silberberg et al., 2016) suggest the existence of two pools of PV$^+$ GPe neurons that are produced with different temporal patterns and occupy slightly different, but otherwise largely overlapping spatial domains within the GPe. Consistent with this observation, more recent single-cell transcriptomic analysis confirms the existence of four major neuron types in the GPe, including two PV$^+$ neuron clusters, in addition to two distinct Npas1$^+$ neuron clusters (Saunders et al., 2018). It is paramount to determine whether they constitute distinct functional subclasses. These efforts will, in turn, give meaning to otherwise arbitrary classifications.

Classification of GPe neurons

Heterogeneity in phenotype of GPe neurons was noted in the early 70's (DeLong, 1971; Fox et al., 1974). The descriptions of molecularly-defined GPe neuron subtypes were not established until less than a decade ago (Flandin et al., 2010; Nobrega-Pereira et al., 2010). Our group has extended previous findings that PV$^+$ neurons and Npas1$^+$ neurons represent the two neuron classes in the adult GPe. Specifically, these two neuron classes are distinct across multiple modalities, including axonal patterns, electrophysiological properties, and alterations in disease states (Glajch et al., 2016; Hegeman et al., 2016; Hernandez et al., 2015). Our unpublished observations (Pamucku, Cui, Berceau, and Chan) continue to support this notion; in particular, the synaptic inputs to PV$^+$ neurons and Npas1$^+$ neurons are distinct. On the other hand, other groups have adopted different, though not mutually exclusive, classification schemes.

Within the Npas1$^+$ class, Foxp2$^+$ neurons (Npas1$^+$-Foxp2$^+$, aka arkypallidal neurons) represent the first unique GPe neuron subclass to be described. This idea is supported by compelling data showing their distinct features, such as developmental origin, electrophysiological, anatomical, and molecular profiles (Dodson et al., 2015). Based on relative spike timing across basal ganglia nuclei in an operant behavioral task, it is suggestive that Npas1$^+$-Foxp2$^+$ neurons are important for motor suppression (Mallet et al., 2016). Meanwhile, the makeup of the remaining neurons in the GPe has been elusive. They are commonly referred to as prototypic neurons. We

(this study) and others noted that prototypic neurons are not simply a single class of neurons (Abdi et al., 2015; Abrahao and Lovinger, 2018; Dodson et al., 2015; Flandin et al., 2010; Hunt et al., 2018; Mastro et al., 2014; Nobrega-Pereira et al., 2010; Oh et al., 2017; Saunders et al., 2018; Saunders et al., 2015). Instead, this group encompasses a heterogeneous population of neurons, and their properties remain to be fully described. Our incomplete understanding of these neurons have prevented us from appreciating how individual neuron subclasses are precisely involved in motor function and dysfunction.

What is a cell type?

We have used 'subset', 'subtype', 'subclass' in this study to best describe our results. To date, there is no common convention in the field on how these terms should be defined. In this study, 'subset' is used strictly as a numerical descriptor with no biological context; 'subtype' and 'type' are used interchangeably when neurons are discussed within the context of a specific set of molecularly- or phenotypically-defined neurons; 'subclasses' is reserved for the use of defining a distinct functional set of neurons that are a constituent subtype within the PV^+ class or $Npas1^+$ class. They are expected to form unique circuit modules and help achieve a complex behavioral repertoire.

Defining a *bona fide* functional cell type presents a challenging question. The classification of neurons can be based on a number of modalities, such as birthplace/date, transcriptome, connectome, intrinsic properties, and their involvements in behavioral and disease context. There are different grouping methods depending on the dimension of analysis and if measurements are categorical. For example, the $Npas1^+$ neuron class in the GPe can be classified as arkypallidal and prototypic, depending on their respective expression of Foxp2 and Nkx2.1. As we begin to learn about GPe neurons and their properties, the classification scheme should continue to evolve in an iterative manner.

Importantly, local environment (created by complex cell-cell interactions between both neuron and glia), physiological states, and experience-dependent plasticity all lead to biological variations in gene and protein expression within and across neuron subclasses and further obscure distinctions between them (Dehorter et al., 2015; Flavell and Greenberg, 2008; Spitzer, 2015, 2017). In both current and past studies (Glajch et al., 2016;

Hegeman et al., 2016; Hernandez et al., 2015), we assert that PV$^+$ neurons and Npas1$^+$ neurons are the two GPe neuron classes. While we have no prior information on whether PV and Npas1 are constitutive components of the cellular steady-state, we should be cautious of the distinction between neuron classes as that may explain the discrepancies across studies. We hope in the future to identify molecular markers that are constant versus those that vary with the states or experiences of test subjects. In addition to examining the expression of classic transcription factors, our increasing knowledge about enhancer elements, terminal selectors, epigenetic modifications, and transcriptional maintenance will help refine the classification of neurons.

Concluding remarks

In this study, we have attempted the characterization of various driver and reporter lines. We hope that our findings will facilitate cross-laboratory utilization of standard tools to study GPe neuron types. The identification of GPe neurons should allow experiments to be conducted on the same neuron type across subjects and laboratories. Examining the same (i.e. homologous) neuron population across species facilitates comparative studies; commonalities and differences in phenotype could then be linked to behavior. As we have completed cataloging major neuron types within the GPe, our next goal is to use intersectional tools to define constituent neuron subclasses and their functions. We have used similar strategies in this study and also recently in Poulin et al. (Poulin et al., 2018). The generation and identification of additional Flp driver lines will likely be helpful for the interrogation of GPe neuron diversity and function. Ultimately, our goal is to identify single recombinase driver lines that efficiently capture functional neuron subclasses.

References

Abdi A, Mallet N, Mohamed FY, Sharott A, Dodson PD, Nakamura KC, Suri S, Avery SV, Larvin JT, Garas FN, Garas SN, Vinciati F, Morin S, Bezard E, Baufreton J, Magill PJ (2015) Prototypic and arkypallidal neurons in the dopamine-intact external globus pallidus. The Journal of neuroscience : the official journal of the Society for Neuroscience 35:6667-6688.

Abrahao KP, Lovinger DM (2018) Classification of GABAergic neuron subtypes from the globus pallidus using wild-type and transgenic mice. The Journal of physiology 596:4219-4235.

Ahrlund-Richter S, Xuan Y, van Lunteren JA, Kim H, Ortiz C, Pollak Dorocic I, Meletis K, Carlen M (2019) A whole-brain atlas of monosynaptic input targeting four different cell types in the medial prefrontal cortex of the mouse. Nature neuroscience 22:657-668.

Anderson ME, Horak FB (1985) Influence of the globus pallidus on arm movements in monkeys. III. Timing of movement-related information. Journal of neurophysiology 54:433-448.

Anderson SA, Marin O, Horn C, Jennings K, Rubenstein JL (2001) Distinct cortical migrations from the medial and lateral ganglionic eminences. Development (Cambridge, England) 128:353-363.

Asanuma C (1989) Axonal arborizations of a magnocellular basal nucleus input and their relation to the neurons in the thalamic reticular nucleus of rats. Proceedings of the National Academy of Sciences of the United States of America 86:4746-4750.

Asanuma C (1994) GABAergic and pallidal terminals in the thalamic reticular nucleus of squirrel monkeys. Experimental brain research 101:439-451.

Azim E, Jabaudon D, Fame RM, Macklis JD (2009) SOX6 controls dorsal progenitor identity and interneuron diversity during neocortical development. Nature neuroscience 12:1238-1247.

Batista-Brito R, Rossignol E, Hjerling-Leffler J, Denaxa M, Wegner M, Lefebvre V, Pachnis V, Fishell G (2009) The cell-intrinsic requirement of Sox6 for cortical interneuron development. Neuron 63:466-481.

Bielle F, Griveau A, Narboux-Neme N, Vigneau S, Sigrist M, Arber S, Wassef M, Pierani A (2005) Multiple origins of Cajal-Retzius cells at the borders of the developing pallium. Nature neuroscience 8:1002-1012.

Butt SJ, Sousa VH, Fuccillo MV, Hjerling-Leffler J, Miyoshi G, Kimura S, Fishell G (2008) The requirement of Nkx2-1 in the temporal specification of cortical interneuron subtypes. Neuron 59:722-732.

Chan CS, Peterson JD, Gertler TS, Glajch KE, Quintana RE, Cui Q, Sebel LE, Plotkin JL, Shen W, Heiman M, Heintz N, Greengard P, Surmeier DJ (2012) Strain-specific regulation of striatal phenotype in Drd2-eGFP BAC transgenic mice. The Journal of neuroscience : the official journal of the Society for Neuroscience 32:9124-9132.

Chen MC, Ferrari L, Sacchet MD, Foland-Ross LC, Qiu MH, Gotlib IH, Fuller PM, Arrigoni E, Lu J (2015) Identification of a direct GABAergic pallidocortical pathway in rodents. The European journal of neuroscience 41:748-759.

Chittajallu R, Craig MT, McFarland A, Yuan X, Gerfen S, Tricoire L, Erkkila B, Barron SC, Lopez CM, Liang BJ, Jeffries BW, Pelkey KA, McBain CJ (2013) Dual origins of functionally distinct O-LM interneurons revealed by differential 5-HT(3A)R expression. Nature neuroscience 16:1598-1607.

Clemente-Perez A, Makinson SR, Higashikubo B, Brovarney S, Cho FS, Urry A, Holden SS, Wimer M, David C, Fenno LE, Acsady L, Deisseroth K, Paz JT (2017) Distinct Thalamic Reticular Cell Types Differentially Modulate Normal and Pathological Cortical Rhythms. Cell reports 19:2130-2142.

Cornwall J, Cooper JD, Phillipson OT (1990) Projections to the rostral reticular thalamic nucleus in the rat. Experimental brain research 80:157-171.

Cui Q, Pitt JE, Pamukcu A, Poulin JF, Mabrouk OS, Fiske MP, Fan IB, Augustine EC, Young KA, Kennedy RT, Awatramani R, Chan CS (2016) Blunted mGluR Activation Disinhibits Striatopallidal Transmission in Parkinsonian Mice. Cell reports 17:2431-2444.

Daigle TL et al. (2018) A Suite of Transgenic Driver and Reporter Mouse Lines with Enhanced Brain-Cell-Type Targeting and Functionality. Cell 174:465-480.e422.

de Carlos JA, Lopez-Mascaraque L, Valverde F (1996) Dynamics of cell migration from the lateral ganglionic eminence in the rat. The Journal of neuroscience : the official journal of the Society for Neuroscience 16:6146-6156.

Dehorter N, Ciceri G, Bartolini G, Lim L, del Pino I, Marin O (2015) Tuning of fast-spiking interneuron properties by an activity-dependent transcriptional switch. Science (New York, NY) 349:1216-1220.

DeLong MR (1971) Activity of pallidal neurons during movement. Journal of neurophysiology 34:414-427.

DeLong MR, Wichmann T (2007) Circuits and circuit disorders of the basal ganglia. Archives of neurology 64:20-24.

Dodson PD, Larvin JT, Duffell JM, Garas FN, Doig NM, Kessaris N, Duguid IC, Bogacz R, Butt SJ, Magill PJ (2015) Distinct developmental origins manifest in the specialized encoding of movement by adult neurons of the external globus pallidus. Neuron 86:501-513.

Du T, Xu Q, Ocbina PJ, Anderson SA (2008) NKX2.1 specifies cortical interneuron fate by activating Lhx6. Development (Cambridge, England) 135:1559-1567.

Flames N, Pla R, Gelman DM, Rubenstein JL, Puelles L, Marin O (2007) Delineation of multiple subpallial progenitor domains by the combinatorial expression of transcriptional codes. The Journal of neuroscience : the official journal of the Society for Neuroscience 27:9682-9695.

Flandin P, Kimura S, Rubenstein JL (2010) The progenitor zone of the ventral medial ganglionic eminence requires Nkx2-1 to generate most of the globus pallidus but few neocortical interneurons. The Journal of neuroscience : the official journal of the Society for Neuroscience 30:2812-2823.

Flavell SW, Greenberg ME (2008) Signaling mechanisms linking neuronal activity to gene expression and plasticity of the nervous system. Annual review of neuroscience 31:563-590.

Fogarty M, Grist M, Gelman D, Marin O, Pachnis V, Kessaris N (2007) Spatial genetic patterning of the embryonic neuroepithelium generates GABAergic interneuron diversity in the adult cortex. The Journal of neuroscience : the official journal of the Society for Neuroscience 27:10935-10946.

Fox CA, Andrade AN, Lu Qui IJ, Rafols JA (1974) The primate globus pallidus: a Golgi and electron microscopic study. Journal fur Hirnforschung 15:75-93.

Gandia JA, De Las Heras S, Garcia M, Gimenez-Amaya JM (1993) Afferent projections to the reticular thalamic nucleus from the globus pallidus and the substantia nigra in the rat. Brain research bulletin 32:351-358.

Gelman D, Griveau A, Dehorter N, Teissier A, Varela C, Pla R, Pierani A, Marin O (2011) A wide diversity of cortical GABAergic interneurons derives from the embryonic preoptic area. The Journal of neuroscience : the official journal of the Society for Neuroscience 31:16570-16580.

Gelman DM, Martini FJ, Nobrega-Pereira S, Pierani A, Kessaris N, Marin O (2009) The embryonic preoptic area is a novel source of cortical GABAergic interneurons. The Journal of neuroscience : the official journal of the Society for Neuroscience 29:9380-9389.

Glajch KE, Kelver DA, Hegeman DJ, Cui Q, Xenias HS, Augustine EC, Hernandez VM, Verma N, Huang TY, Luo M, Justice NJ, Chan CS (2016) Npas1+ Pallidal Neurons Target Striatal Projection Neurons. The Journal of neuroscience : the official journal of the Society for Neuroscience 36:5472-5488.

Graybiel AM (2008) Habits, rituals, and the evaluative brain. Annual review of neuroscience 31:359-387.

Harris JA, Hirokawa KE, Sorensen SA, Gu H, Mills M, Ng LL, Bohn P, Mortrud M, Ouellette B, Kidney J, Smith KA, Dang C, Sunkin S, Bernard A, Oh SW, Madisen L, Zeng H (2014) Anatomical characterization of Cre driver mice for neural circuit mapping and manipulation. Frontiers in neural circuits 8:76.

Harris KD, Shepherd GM (2015) The neocortical circuit: themes and variations. Nature neuroscience 18:170-181.

Hazrati LN, Parent A (1991) Projection from the external pallidum to the reticular thalamic nucleus in the squirrel monkey. Brain research 550:142-146.

Hegeman DJ, Hong ES, Hernandez VM, Chan CS (2016) The external globus pallidus: progress and perspectives. The European journal of neuroscience 43:1239-1265.

Hernandez VM, Hegeman DJ, Cui Q, Kelver DA, Fiske MP, Glajch KE, Pitt JE, Huang TY, Justice NJ, Chan CS (2015) Parvalbumin+ Neurons and Npas1+ Neurons Are Distinct Neuron Classes in the Mouse External Globus Pallidus. The Journal of neuroscience : the official journal of the Society for Neuroscience 35:11830-11847.

Huang ZJ, Di Cristo G, Ango F (2007) Development of GABA innervation in the cerebral and cerebellar cortices. Nature reviews Neuroscience 8:673-686.

Hunt AJ, Jr., Dasgupta R, Rajamanickam S, Jiang Z, Beierlein M, Chan CS, Justice NJ (2018) Paraventricular hypothalamic and amygdalar CRF neurons synapse in the external globus pallidus. Brain structure & function 223:2685-2698.

Ito M, Doya K (2011) Multiple representations and algorithms for reinforcement learning in the cortico-basal ganglia circuit. Current opinion in neurobiology 21:368-373.

Jaeger D, Kita H (2011) Functional connectivity and integrative properties of globus pallidus neurons. Neuroscience 198:44-53.

Jaglin XH, Hjerling-Leffler J, Fishell G, Batista-Brito R (2012) The origin of neocortical nitric oxide synthase-expressing inhibitory neurons. Frontiers in neural circuits 6:44.

Jahanshahi M, Obeso I, Rothwell JC, Obeso JA (2015) A fronto-striato-subthalamic-pallidal network for goal-directed and habitual inhibition. Nature reviews Neuroscience 16:719-732.

Jimenez D, Lopez-Mascaraque LM, Valverde F, De Carlos JA (2002) Tangential migration in neocortical development. Developmental biology 244:155-169.

Jin X, Tecuapetla F, Costa RM (2014) Basal ganglia subcircuits distinctively encode the parsing and concatenation of action sequences. Nature neuroscience 17:423-430.

Kanki H, Suzuki H, Itohara S (2006) High-efficiency CAG-FLPe deleter mice in C57BL/6J background. Experimental animals 55:137-141.

Kayahara T, Nakano K (1998) The globus pallidus sends axons to the thalamic reticular nucleus neurons projecting to the centromedian nucleus of the thalamus: a light and electron microscope study in the cat. Brain research bulletin 45:623-630.

Kim Y, Yang GR, Pradhan K, Venkataraju KU, Bota M, Garcia Del Molino LC, Fitzgerald G, Ram K, He M, Levine JM, Mitra P, Huang ZJ, Wang XJ, Osten P (2017) Brain-wide Maps Reveal Stereotyped Cell-Type-Based Cortical Architecture and Subcortical Sexual Dimorphism. Cell 171:456-469.e422.

Kita H (2007) Globus pallidus external segment. Progress in brain research 160:111-133.

Klaus A, da Silva JA, Costa RM (2019) What, If, and When to Move: Basal Ganglia Circuits and Self-Paced Action Initiation. Annual review of neuroscience.

Knowland D, Lilascharoen V, Pacia CP, Shin S, Wang EH, Lim BK (2017) Distinct Ventral Pallidal Neural Populations Mediate Separate Symptoms of Depression. Cell 170:284-297.e218.

Krzywinski M, Altman N (2014) Visualizing samples with box plots. Nature methods 11:119-120.

Liodis P, Denaxa M, Grigoriou M, Akufo-Addo C, Yanagawa Y, Pachnis V (2007) Lhx6 activity is required for the normal migration and specification of cortical interneuron subtypes. The Journal of neuroscience : the official journal of the Society for Neuroscience 27:3078-3089.

Mallet N, Schmidt R, Leventhal D, Chen F, Amer N, Boraud T, Berke JD (2016) Arkypallidal Cells Send a Stop Signal to Striatum. Neuron 89:308-316.

Mandelbaum G, Taranda J, Haynes TM, Hochbaum DR, Huang KW, Hyun M, Umadevi Venkataraju K, Straub C, Wang W, Robertson K, Osten P, Sabatini BL (2019) Distinct Cortical-Thalamic-Striatal Circuits through the Parafascicular Nucleus. Neuron 102:636-652.e637.

Mastro KJ, Bouchard RS, Holt HA, Gittis AH (2014) Transgenic mouse lines subdivide external segment of the globus pallidus (GPe) neurons and reveal distinct GPe output pathways. The Journal of neuroscience : the official journal of the Society for Neuroscience 34:2087-2099.

Mastro KJ, Zitelli KT, Willard AM, Leblanc KH, Kravitz AV, Gittis AH (2017) Cell-specific pallidal intervention induces long-lasting motor recovery in dopamine-depleted mice. Nature neuroscience 20:815-823.

Mink JW (1996) The basal ganglia: focused selection and inhibition of competing motor programs. Progress in neurobiology 50:381-425.

Nambu A, Tachibana Y (2014) Mechanism of parkinsonian neuronal oscillations in the primate basal ganglia: some considerations based on our recent work. Frontiers in systems neuroscience 8:74.

Nobrega-Pereira S, Gelman D, Bartolini G, Pla R, Pierani A, Marin O (2010) Origin and molecular specification of globus pallidus neurons. The Journal of neuroscience : the official journal of the Society for Neuroscience 30:2824-2834.

Oh YM, Karube F, Takahashi S, Kobayashi K, Takada M, Uchigashima M, Watanabe M, Nishizawa K, Kobayashi K, Fujiyama F (2017) Using a novel PV-Cre rat model to characterize pallidonigral cells and their terminations. Brain structure & function 222:2359-2378.

Pazo JH, Barcelo AC, Bellantonio E, Pazo VC, Almarares N (2013) Electrophysiologic study of globus pallidus projections to the thalamic reticular nucleus. Brain research bulletin 94:82-89.

Poulin JF, Caronia G, Hofer C, Cui Q, Helm B, Ramakrishnan C, Chan CS, Dombeck DA, Deisseroth K, Awatramani R (2018) Mapping projections of molecularly defined dopamine neuron subtypes using intersectional genetic approaches. Nature neuroscience 21:1260-1271.

Redgrave P, Rodriguez M, Smith Y, Rodriguez-Oroz MC, Lehericy S, Bergman H, Agid Y, DeLong MR, Obeso JA (2010) Goal-directed and habitual control in the basal ganglia: implications for Parkinson's disease. Nature reviews Neuroscience 11:760-772.

Rubenstein JL, Shimamura K, Martinez S, Puelles L (1998) Regionalization of the prosencephalic neural plate. Annual review of neuroscience 21:445-477.

Saunders A, Oldenburg IA, Berezovskii VK, Johnson CA, Kingery ND, Elliott HL, Xie T, Gerfen CR, Sabatini BL (2015) A direct GABAergic output from the basal ganglia to frontal cortex. Nature 521:85-89.

Saunders A, Macosko EZ, Wysoker A, Goldman M, Krienen FM, de Rivera H, Bien E, Baum M, Bortolin L, Wang S, Goeva A, Nemesh J, Kamitaki N, Brumbaugh S, Kulp D, McCarroll SA (2018) Molecular Diversity and Specializations among the Cells of the Adult Mouse Brain. Cell 174:1015-1030.e1016.

Schindelin J, Arganda-Carreras I, Frise E, Kaynig V, Longair M, Pietzsch T, Preibisch S, Rueden C, Saalfeld S, Schmid B, Tinevez JY, White DJ, Hartenstein V, Eliceiri K, Tomancak P, Cardona A (2012) Fiji: an open-source platform for biological-image analysis. Nature methods 9:676-682.

Schwarz LA, Miyamichi K, Gao XJ, Beier KT, Weissbourd B, DeLoach KE, Ren J, Ibanes S, Malenka RC, Kremer EJ, Luo L (2015) Viral-genetic tracing of the input-output organization of a central noradrenaline circuit. Nature 524:88-92.

Shammah-Lagnado SJ, Alheid GF, Heimer L (1996) Efferent connections of the caudal part of the globus pallidus in the rat. The Journal of comparative neurology 376:489-507.

Sherman SM (2016) Thalamus plays a central role in ongoing cortical functioning. Nature neuroscience 19:533-541.

Shi LH, Luo F, Woodward DJ, Chang JY (2004) Neural responses in multiple basal ganglia regions during spontaneous and treadmill locomotion tasks in rats. Experimental brain research 157:303-314.

Silberberg SN, Taher L, Lindtner S, Sandberg M, Nord AS, Vogt D, McKinsey GL, Hoch R, Pattabiraman K, Zhang D, Ferran JL, Rajkovic A, Golonzhka O, Kim C, Zeng H, Puelles L, Visel A, Rubenstein JLR (2016) Subpallial Enhancer Transgenic Lines: a Data and Tool Resource to Study Transcriptional Regulation of GABAergic Cell Fate. Neuron 92:59-74.

Spitzer NC (2015) Neurotransmitter Switching? No Surprise. Neuron 86:1131-1144.

Spitzer NC (2017) Neurotransmitter Switching in the Developing and Adult Brain. Annual review of neuroscience 40:1-19.

Streit M, Gehlenborg N (2014) Bar charts and box plots. Nature methods 11:117.

Sussel L, Marin O, Kimura S, Rubenstein JL (1999) Loss of Nkx2.1 homeobox gene function results in a ventral to dorsal molecular respecification within the basal telencephalon: evidence for a transformation of the pallidum into the striatum. Development (Cambridge, England) 126:3359-3370.

Tamamaki N, Fujimori KE, Takauji R (1997) Origin and route of tangentially migrating neurons in the developing neocortical intermediate zone. The Journal of neuroscience : the official journal of the Society for Neuroscience 17:8313-8323.

Turner RS, Anderson ME (2005) Context-dependent modulation of movement-related discharge in the primate globus pallidus. The Journal of neuroscience : the official journal of the Society for Neuroscience 25:2965-2976.

Wamsley B, Fishell G (2017) Genetic and activity-dependent mechanisms underlying interneuron diversity. Nature reviews Neuroscience 18:299-309.

Xu Q, Tam M, Anderson SA (2008) Fate mapping Nkx2.1-lineage cells in the mouse telencephalon. The Journal of comparative neurology 506:16-29.

Yetman MJ, Washburn E, Hyun JH, Osakada F, Hayano Y, Zeng H, Callaway EM, Kwon HB, Taniguchi H (2019) Intersectional monosynaptic tracing for dissecting subtype-specific organization of GABAergic interneuron inputs. Nature neuroscience 22:492-502.

Zeisel A, Hochgerner H, Lonnerberg P, Johnsson A, Memic F, van der Zwan J, Haring M, Braun E, Borm LE, La Manno G, Codeluppi S, Furlan A, Lee K, Skene N, Harris KD, Hjerling-Leffler J, Arenas E, Ernfors P, Marklund U, Linnarsson S (2018) Molecular Architecture of the Mouse Nervous System. Cell 174:999-1014.e1022.

Figure Legends

Figure 1. GPe neuron diversity.

a. The location of the GPe in a mouse brain is illustrated (side view). **b**. GPe neurons at three different lateral, intermediate, and medial levels (~2.5, 2.1, and 1.7 lateral from bregma) were sampled. **c**. Using HuCD as a neuronal marker, population data for the relative abundance of GPe neuron markers was determined. Inset: low magnification confocal image of HuCD-labeling in the GPe with the dStr and ic denoting the rostral and caudal borders of the GPe, respectively. **d**. Low magnification confocal images of the GPe and TRN in PV-L-tdTom (PV-Cre;LSL-tdTomato) and PV-tdTom BAC mice. **e**. PV-F-tdTom (PV-Flp;FSF-tdTomato) and Nkx2.1-F-tdTom (Nkx2.1-Flp;FSF-tdTomato) were used in this study. The PV-F-tdTom (PV-Flp;FSF-tdTomato) transgenic mouse line produces faithful reporting of PV^+ neurons and similar cytoplasmic neuron labeling as the PV-L-tdTom and PV-tdTom BAC lines (as shown in **d**). Top, low magnification showing the PV-F-tdTom line produces prominent tdTomato-expression ($tdTomato^+$) in PV^+ neurons in the TRN in addition to the GPe. To confirm the validity of the mouse line, tdTomato expression was compared against PV immunostaining. A higher magnification of the GPe shows nearly all $tdTomato^+$ (magenta) neurons colocalize with PV-ir (green). Bottom, Nkx2.1-F-tdTom reliably captures neurons that arise from the Nkx2.1 lineage. Note that no cell bodies were found in the TRN (see also, Figure **5f**). Double immunolabeling with tdTomato and Nkx2.1 demonstrated ~90% colocalization. Arrowheads indicate neurons that do not colocalize. **f**. Triple immunostaining with PV, Npas1, and GFP on Lhx6-GFP brain sections confirms the existence of a $Lhx6^+$-PV^--$Npas1^-$ GPe population. This same population lacks Sox6 expression. Circles indicate $Lhx6^+$ neurons that colocalize with either PV or Npas1. Arrowheads point to unique $Lhx6^+$ neurons. **g**. $Sox6^+$ neurons express established GPe markers. Note that there are both bright and dim populations of $Sox6^+$ neurons. Bottom, arrowheads indicate $Lhx6^+$-$Sox6^-$ neurons. Abbreviations: dStr = dorsal striatum; TRN = thalamic reticular nucleus; VPL/VPM = ventral posterior nucleus; ic = internal capsule.

Figure 2. Lhx6$^+$ and Dbx1$^+$ GPe neurons colocalize with established GPe markers.

a. Left, low and high magnification images of PV$^+$, Sox6$^+$, and Lhx6$^+$ (GFP$^+$) GPe neurons. Right, low and high magnification images of Npas1$^+$, Sox6$^+$, and Lhx6$^+$ (GFP$^+$) GPe neurons. **b**. *In situ* hybridization signals from Dbx1-L-tdTom mouse line for tdTomato$^+$ and Cre$^+$ in the adult GPe and neighboring areas (left). Note the widespread tdTomato$^+$ across brain areas (top right) result from the cumulative recombination from early developmental stages in spite of the absence of Cre$^+$ expression in adult (bottom right). Data are adopted from Allen Brain Atlas. The Dbx1-L-tdTom mouse line labels Dbx1$^+$ (tdTomato$^+$) neurons (HuCD, magenta) and glia in the GPe. **c**. Dbx1$^+$ GPe neurons colocalize with established GPe markers and are largely PV$^+$. Note that there is no overlap between Dbx1 and Foxp2. Circles indicate colocalization, star (bottom right) presents an example of astrocytic labeling in the Dbx1-L-tdTom mouse line. Abbreviations: dStr = dorsal striatum; GPi = internal globus pallidus; SI = substantia innominata; TRN = thalamic reticular nucleus; ac = anterior commissure; ic = internal capsule.

Figure 3. Retrograde tracing analysis.

a. Representative injection sites from retrograde tracing connectome analysis. LVretro-Cre (LV, red) in combination with CTb (green) was injected into dStr (top left), STN (top right), SNr (bottom right) and mounted with DAPI (blue) to visualize cytoarchitecture. **b**. Retrograde labeling of GPe-STN and GPe-dStr neurons with both LV and CTb tracing techniques. CTb (top left, green) labeled and LV (bottom left) GPe neurons from STN injection are substantially PV$^+$ (magenta) and do not colocalize with Npas1 immunostaining (bottom right). CTb (top right, green) labeled GPe neurons from dStr injection with Npas1 immunostaining (magenta). **c**. Retrograde labeling in Dbx1-L-tdTom mice shows Dbx1$^+$ neurons (magenta) project to STN (top left) and SNr (top right) as indicated by colocalization with CTb retrobeads (green). Arrowheads denote CTb$^+$ STN projecting neurons that lack expression of Dbx1. Bottom left, coronal view of a representative injection to the PF (left) along with expected positive cortical fluorescence (MO, right). No fluorescence was observed in the GPe. Abbreviations: dStr = dorsal striatum; Ctx = cortex; GPe = external globus pallidus; GPi = internal globus pallidus; Hp = hippocampus; PF = parafascicular nucleus; LGd = lateral geniculate, dorsal; MO = somatosensory cortex; SI = substantia innominata; SNr =

substantia nigra pars reticulata; STN = subthalamic nucleus; TRN = thalamic reticular nucleus; ZI = zona incerta; ac = anterior commissure; cpd = cerebral peduncle; ic = internal capsule.

Figure 4. Ctx-GPe-Ctx macroscopic anatomy.

a. Different cortical subregions examined in this study are highlighted. For clarity, frontal (top) and horizontal (bottom) views are shown. **b**. A confocal micrograph showing a representative example of retrogradely-labeled cortex-projecting GPe neurons (arrowhead) using LVreto-Cre in a LSL-tdTomato mouse PV-immunohistological labeling (green) was performed in this example. Inset: experimental setup. LVretro-Cre and CTb were injected into different cortical areas mentioned in **a**. **c**. Top left, experimental setup: LVretro-Cre and CTb were injected into the GPe. Cortical inputs to the GPe were mapped using two-photon tomography. Top right, a two-photon image showing the location of the injection site. Bottom, representative two-photon images from coronal sections showing GPe-projecting cortical neurons were found primarily in layer 5 and 6 of MO and SS. **d**. Left, quantification of retrogradely-labeled GPe neurons from frontal cortical regions (i.e., ORB, MOp, SSp). Right, quantification of brain-wide input to the GPe. Medians, interquartile ranges, and 10^{th} to 90^{th} percentiles are represented in a graphical format. **e**. Low magnification image of $Npas1^{+}$ GPe-Ctx axons spanning across ORB, MO, and SS. Note the highest density occurs in layers 5 and 6 of MO followed by SS and drops off precipitately rostrally in the ORB. Axons extend as far as layer 2/3. **f**. Local cortical infection in a Npas1-Cre-tdTom mouse confirms axons visible in rostral cortical regions cortex are from GPe projection and not ectopic infection of cortical neurons in the caudal areas. Injection site into SS (left) and rostral MO and ORB (right) showing very low density of caudal to rostral cortical-cortical connectivity. Arrowheads indicate the presence of cortical axons that arose from the more caudal regions. Abbreviations: dStr = dorsal striatum; CLA = claustrum; MOp = primary somatosensory; MOs = secondary somatosensory; ORB = orbital; Sp = septum; SSp-n = primary somatosensory, nose; SSp-bfd = primary somatosensory, barrel field; SSp-ll = primary somatosensory, lower limb; SSp-m = primary somatosensory, mouth; SSp-ul = primary somatosensory, upper limb; SSp-tr = primary somatosensory, trunk; SSs = secondary somatosensory; VISC = visceral; ac = anterior commissure; cc = corpus callosum; fa = anterior forceps.

Figure 5. Cortex-projecting neuron properties.

a. LV retrograde labeled (magenta) GPe neurons with PV immunostaining (green). Note, cortical projecting GPe neurons are not PV^+. Arrowhead indicates a LV labeled neuron with a large cell body characteristic of cholinergic neurons. **b**. A confocal micrograph showing the co-expression (dotted circles) of Npas1 (yellow) and Nkx2.1 (blue) in cortex-projecting GPe neurons (magenta). Inset: same mag, an example of a neuron that has large cell body and low Nkx2.1 expression, features of cholinergic neurons within the confines of the GPe. **c**. High magnification confocal micrographs of axons in the Ctx, dStr, and TRN with injection of a CreOn-ChR2 AAV into the GPe of a Npas1-Cre-tdTom mouse. Asterisks in top left denote putative terminals. Bottom right, high density of synaptic boutons in the TRN of Nkx2.1-F-tdTom mice. **d**. Voltage-clamp recordings of the $Npas1^+$ GPe input in a neuron between layers 5 and 6. The recorded neuron was held at –70 mV with a high Cl^- electrode; inhibitory postsynaptic currents (IPSCs) were evoked from 20 Hz paired-pulse blue light stimulation (indicated by gray circles). Note, the fast and depressing responses evoked. Inset: location of the recorded neuron (asterisk) in the cortex (Ctx) is shown. IPSCs were attenuated with extracortical stimulation (not shown) abolished with tetrodotoxin (TTX, 1 μM). Application of 4-aminopyridine (4-AP, 100 μM) in presence of TTX restored the response with intracortical stimulations. IPSCs were completely blocked with SR95531 (10 μM), demonstrating their GABAergic nature. **e**. Voltage-clamp recording of a TRN neuron with identical experimental setup shown in **d**. Note the facilitating responses evoked. Inset: location of the recorded neuron (asterisk) is shown. Responses were sensitive to the application of SR95531 (10 μM). **f**. Left, pie charts summarizing the percentages of responders in Ctx and TRN. Right, medians and interquartile ranges of IPSC amplitude are represented in a graphical format. Abbreviations: dStr = dorsal striatum; Ctx = cortex; TRN = thalamic reticular nucleus; cc = corpus callosum; ic = internal capsule.

Figure 6. Lateromedial gradients and relative abundance of different GPe neuron classes.

a. Spatial maps of the pan $Lhx6^+$ and unique $Lhx6^+$ $Sox6^-$ GPe neuron populations. Both populations display a lateromedial gradient with more neurons populating the medial GPe. **b**. Relative abundance of neuron classes in

different lateromedial subdivisions of the GPe ($Sox6^+$ = lateral: 60 ± 12%, *n* = 4,457 neurons, intermediate: 63 ± 11%, *n* = 5,112 neurons, medial: 50 ± 11%, *n* = 3,286 neurons; $Nkx2.1^+$ = lateral: 56 ± 7%, *n* = 3,365 neurons, intermediate: 53 ± 9%, *n* = 3,878 neurons, medial: 64 ± 14%, *n* = 3,265 neurons; PV^+ = lateral: 46 ± 10%, *n* = 4,368 neurons, intermediate: 45 ± 11%, *n* = 5,113 neurons, medial: 32 ± 7%, *n* = 2,829 neurons; $Lhx6^+$ = lateral: 28 ± 6%, *n* = 1,422 neurons, intermediate: 42 ± 9%, *n* = 2,050 neurons, medial: 45 ± 12%, *n* = 2,190 neurons; $Npas1^+$ = lateral: 33 ± 6%, *n* = 2,635 neurons, intermediate: 31 ± 6%, *n* = 2,903 neurons, medial: 27 ± 7%, *n* = 2,252 neurons; $Foxp2^+$ = lateral: 24 ± 3%, *n* = 939 neurons, intermediate: 26 ± 4%, *n* = 1,115 neurons, medial: 25 ± 6%, *n* = 686 neurons; $Dbx1^+$ = lateral: 10 ± 2%, *n* = 1,219 neurons, intermediate: 9 ± 2%, *n* = 1,540 neurons, medial: 8 ± 2%, *n* = 1,121 neurons; $ChAT^+$ = lateral: 6 ± 1%, *n* = 100 neurons, intermediate: 4 ± 1%, *n* = 76 neurons, medial: 6 ± 3%, *n* = 91 neurons). Percentage total was calculated from $HuCD^+$ cells within each section. Note that PV and Npas1 were expressed in a largely non-overlapping fashion (2 ± 2%, *n* = 96 neurons, 12 sections). In contrast, considerable overlap between Lhx6 and PV (28 ± 7%, *n* = 654 neurons, 12 sections) or Npas1 (35 ± 5%, *n* = 818 neurons, 12 sections) was observed; the remaining fraction was uniquely labeled with Lhx6. Medians and interquartile ranges are represented in a graphical format. Asterisks denote statistical significance level: $^{**}P < 0.01$, Mann-Whitney U test.

Figure 7. Spatial distribution, molecular marker profile, and classification of GPe neurons.

a. Spatial information of GPe neurons cannot be represented relative to bregma location (top, lower left) because of its complex geometry. To mathematically describe the spatial distribution of GPe neurons in each brain section, fixed mouse brains were sagittally sectioned and histologically processed. Images were manually aligned to a reference atlas. GPe neurons located at six different lateromedial levels (2.73 mm, 2.53 mm, 2.35 mm, 2.15 mm, 1.95 mm, and 1.73 mm) were charted and collapsed onto a single plane. As the GPe is similarly-shaped across the lateromedial extent (lower right), both the rostrocaudal and dorsoventral extent are assigned to 0 and 1. The address of each neuron is defined by their x-y coordinates and represented with a marker (black). To capture the aggregate spatial distribution, a geometric centroid (red) of each neuron population was then determined to

represent the center of mass in both x and y dimensions. Centroids are then used as the origin for the polar histograms in b. Size of each sector represent the relative neuron count as a function of direction. **b**. Representative data of neurons from two individual mice are shown in each case, except for retrogradely-labeled cortically-projecting neurons (*n* = 7 mice; 119 neurons; 15 sections). Each marker represents a neuron. The density of neurons are encoded with a yellow-blue gradient. Hash marks, which represent the dorsoventral and rostrocaudal axes, are presented with the centroids and polar histograms to facilitate comparison. Bin sizes in the polar histograms were chosen based on the size of each neuron population. The (x, y) centroid values for the respective GPe distributions were: HuCD$^+$ (0.3798, 0.4168); Nkx2.1$^+$ (0.3599, 0.4439); Sox6$^+$ (0.3587, 0.4529); PV$^+$ (0.3205, 0.4699); Lhx6$^+$ (0.3918, 0.3827); Lhx6$^+$-Sox6$^-$ (0.3755, 0.3164), Dbx1$^+$ (0.3679, 0.3828); ChAT$^+$ (0.6024, 0.3569); Npas1$^+$ (0.4106, 0.4140), Npas1$^+$-Foxp2$^+$ 0.3695, 0.4676); Npas1$^+$-Nkx2.1$^+$ (0.4026, 0.4278); Ctx-projecting GPe neurons (0.5061, 0.2911). **c**. A matrix table describing the prevalence of molecular expression across all identified GPe neuronal subtypes. **d**. A summary of the GPe neuron classification based on the expression profile of different molecular markers. Two *bona fide* Npas1$^+$ neuron subclasses are identified in this study. They displayed unique molecular marker expression profiles.

Figure 8. Identified GPe neurons differ in their autonomous and driven activity.

a. Confocal micrograph showing the expression of mCherry (magenta) resulted from an injection of a CreOn-mCherry AAV into the GPe of Foxp2-cre mice. Immunolabeling for Foxp2 (green) confirmed all mCherry expressing neurons (*n* = 473 out of 485 neurons, 6 sections) were Foxp2$^+$. **b**. Representative brightfield and epifluorescence images of GPe neuron subtypes in *ex vivo* brain slices. Foxp2$^+$ neuron (top, brightfield and mCherry), Lhx6$^+_{bright}$ neurons and Lhx6$^+_{dim}$ (bottom left, GFP), and PV$^+$-Dbx1$^+$ neurons (bottom right, tdTomato) were captured at a 60x magnification. Note the difference in the morphology among Lhx6$^+$ neurons. **c**. Box-plot summary of the electrophysiological properties of identified GPe neuron subtypes. Data are ranked based on the median values. See **Table 5** and **6** for median values, sample sizes, and statistical analysis. Medians, interquartile ranges, and 10th to 90th percentiles are represented in a graphical format.

Figure 9. A diagram summarizing the classification of Npas1$^+$ neuron subclasses.

Two subclasses of Npas1$^+$ neurons (Npas1$^+$-Foxp2$^+$ and Npas1$^+$-Nkx2.1$^+$) are identified in the mouse GPe. They differ in their molecular marker expression, axonal projections, and electrophysiological properties. While Npas1$^+$-Foxp2$^+$ neurons project to the dorsal striatum, Npas1$^+$-Nkx2.1$^+$ neurons project to the cortex, thalamus, and mid/hindbrain areas. It remains unknown if synapses are formed between Npas1$^+$-Nkx2.1$^+$ GPe neurons and the striatum. Size of the target areas (circles) is an artistic representation based on the volume of those areas, but not the axonal density, synaptic strength, or contacts formed by Npas1$^+$ neuron subclasses.

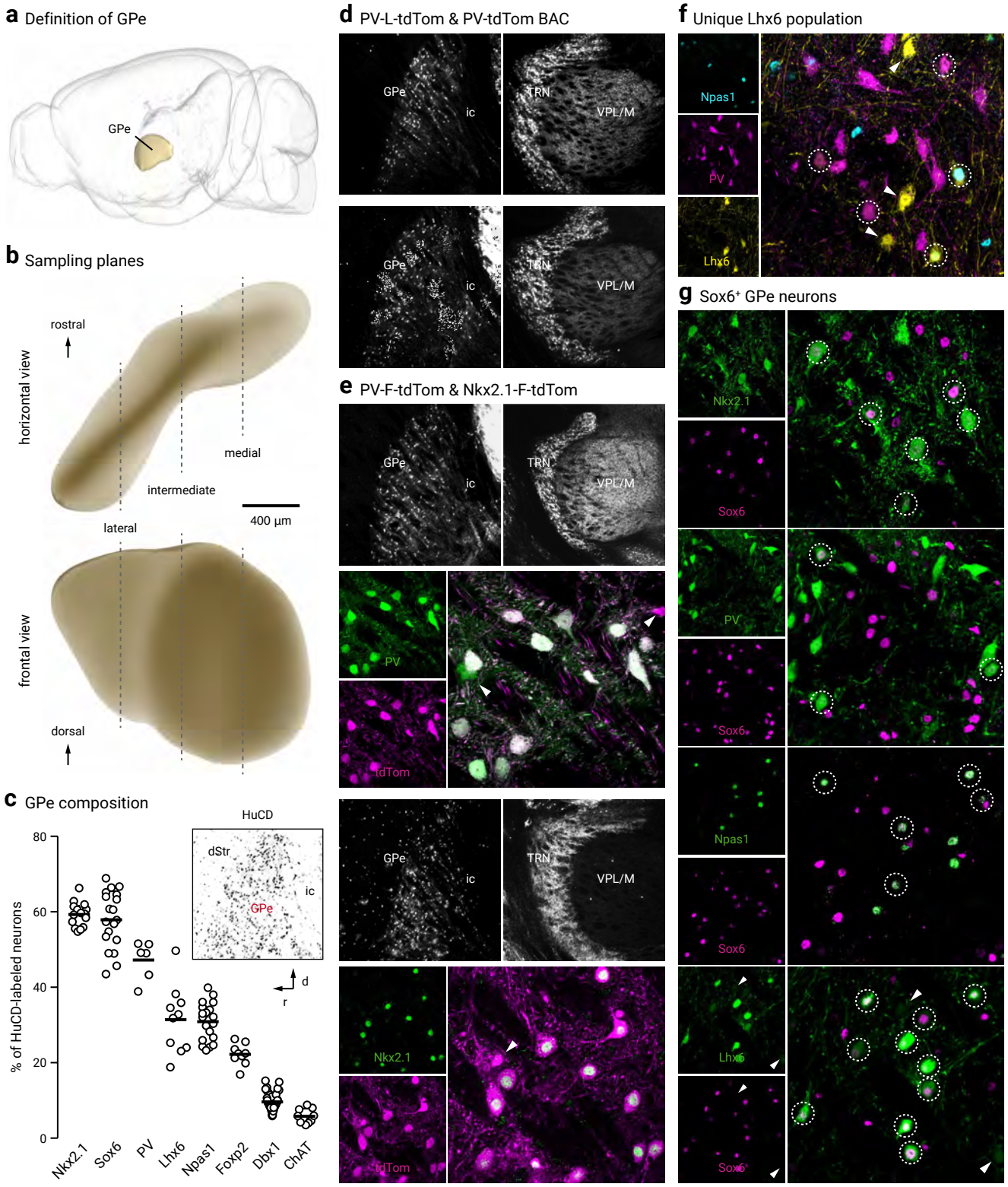

Figure 1

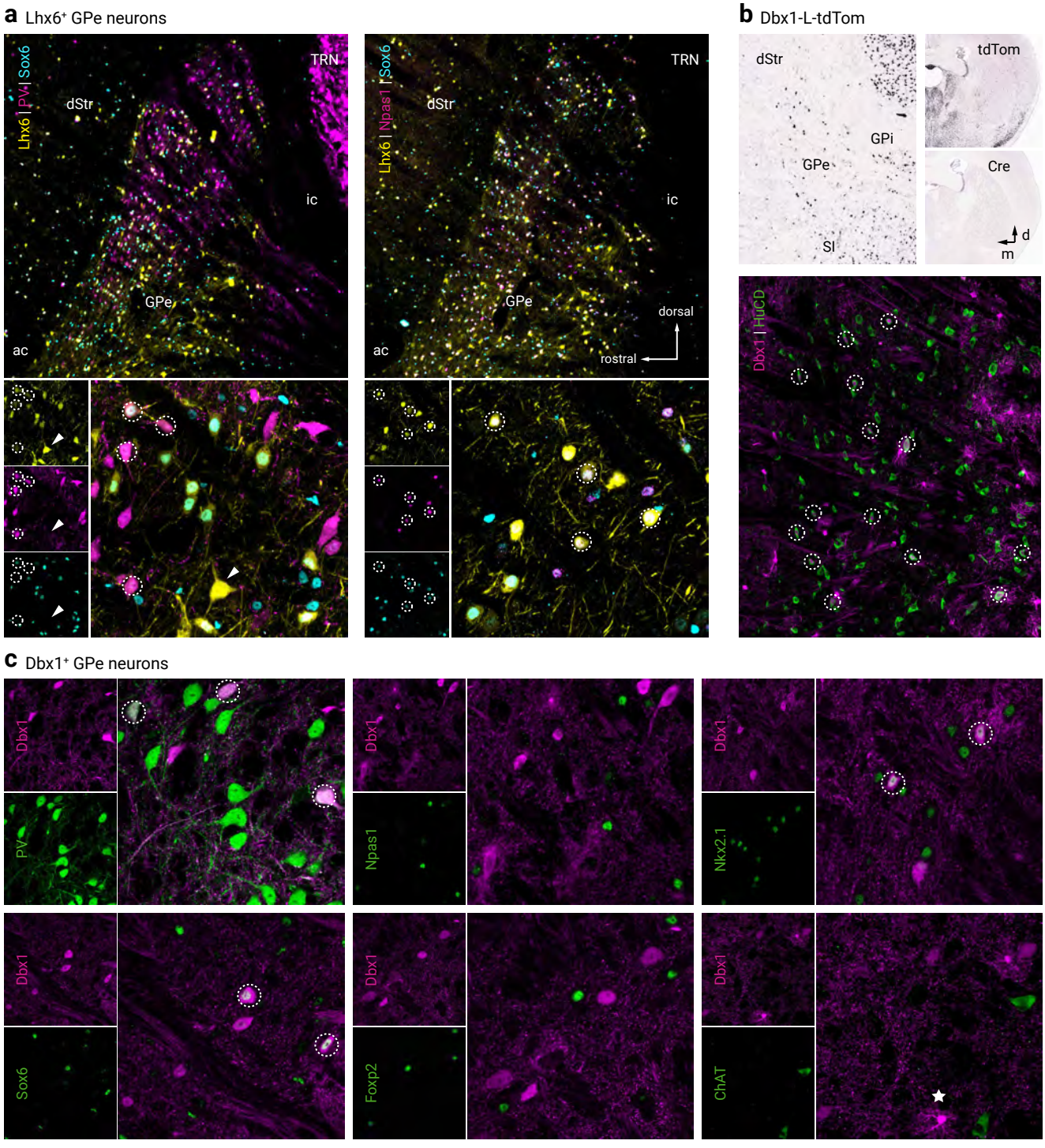

Figure 2

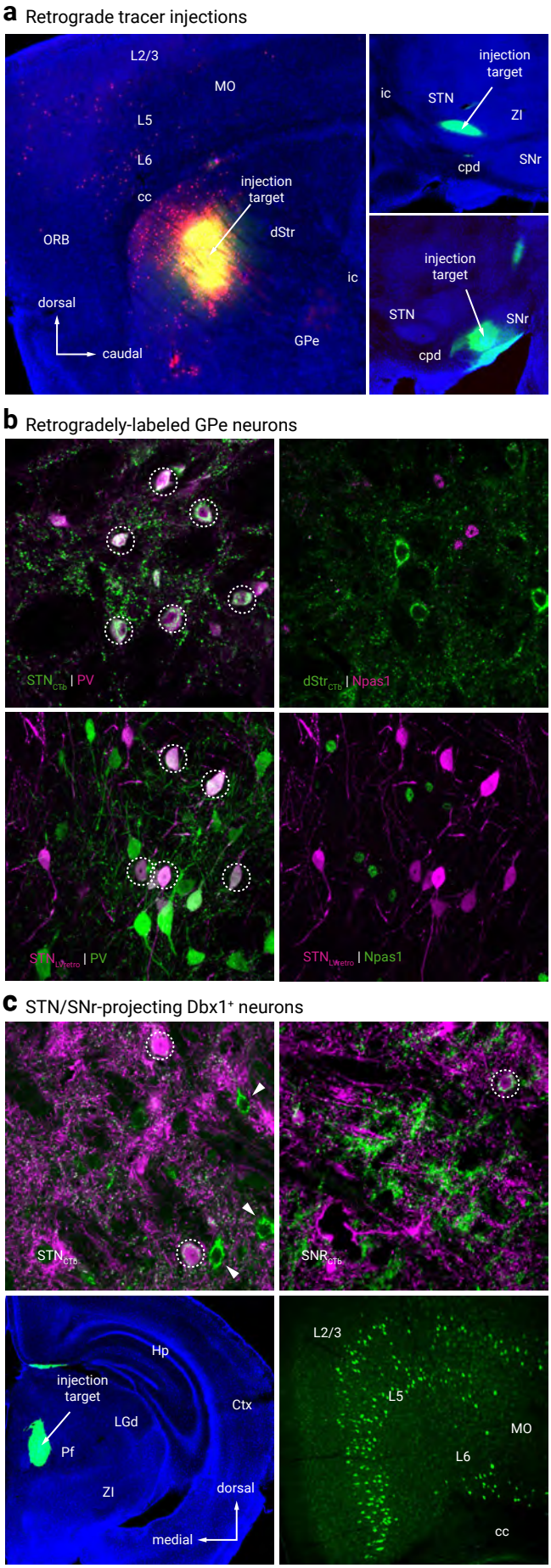

Figure 3

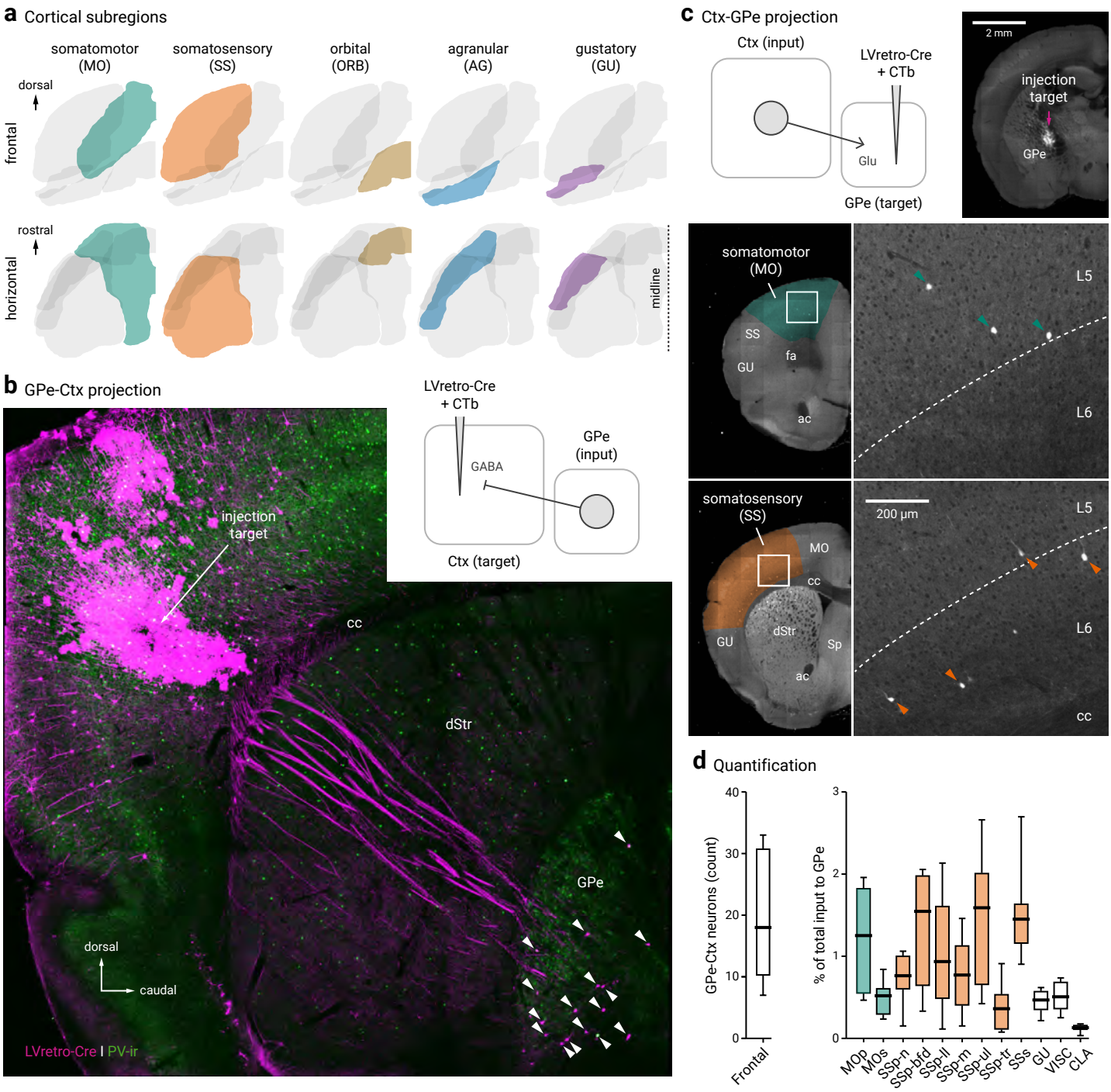

Figure 4

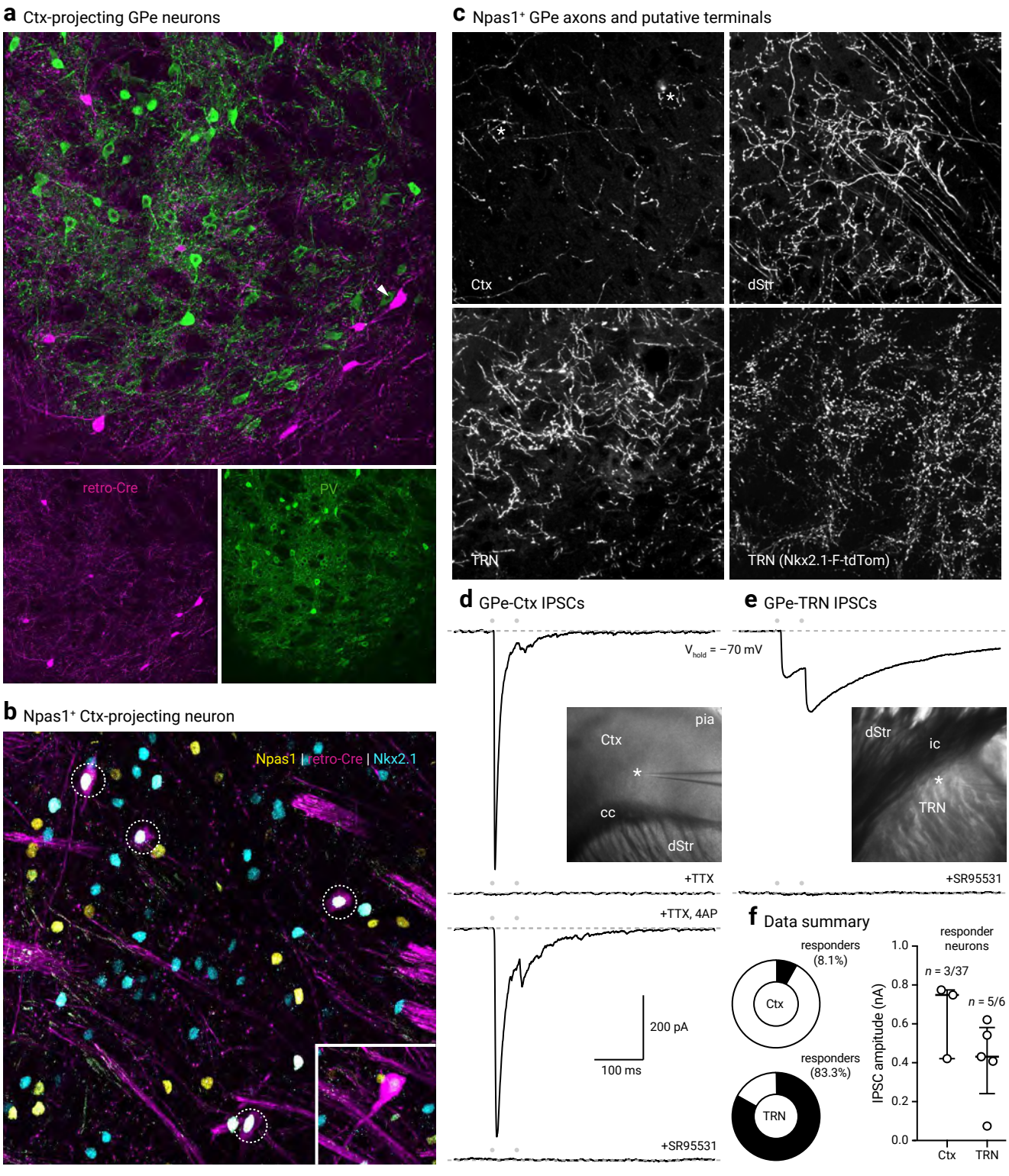

Figure 5

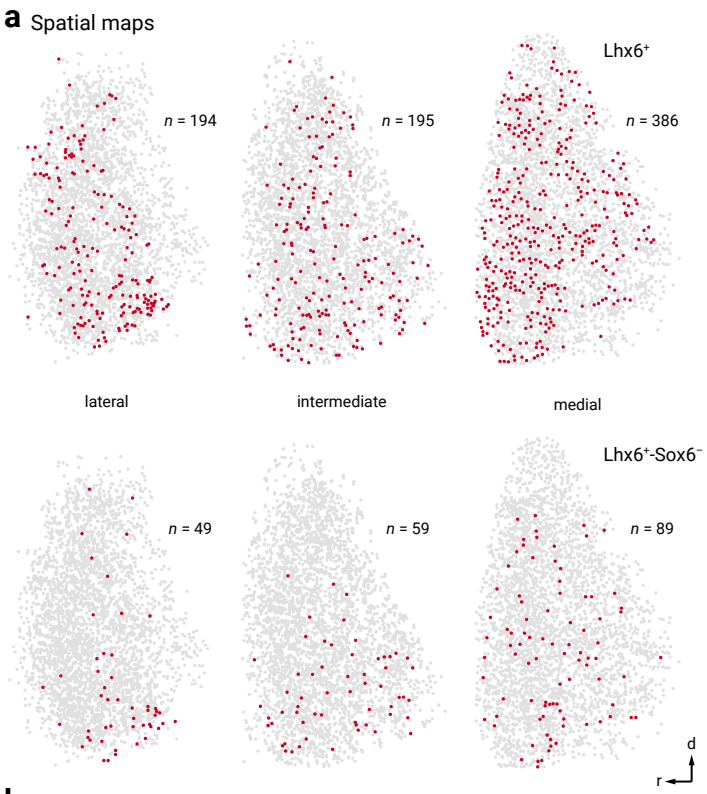

Figure 6

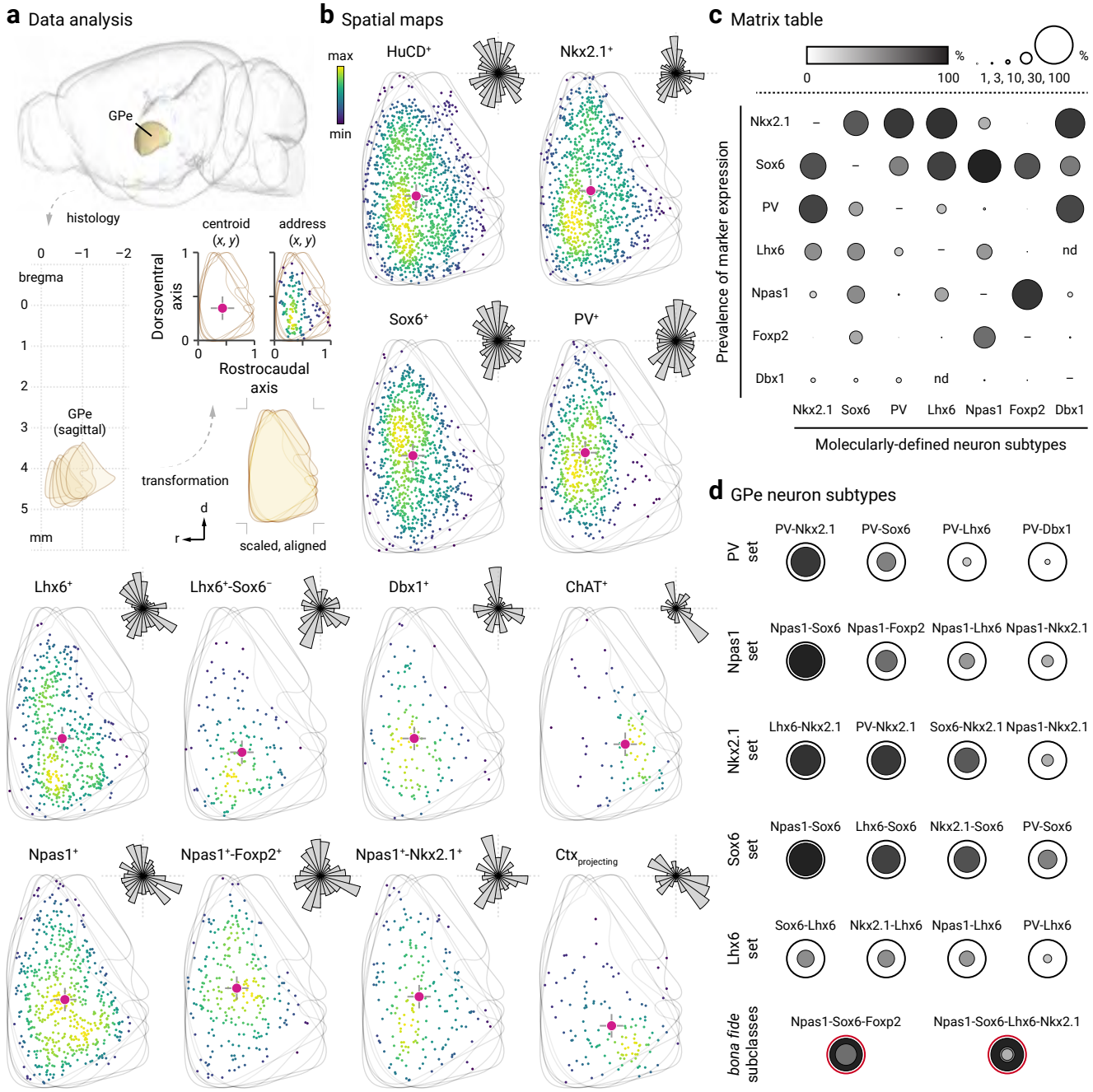

Figure 7

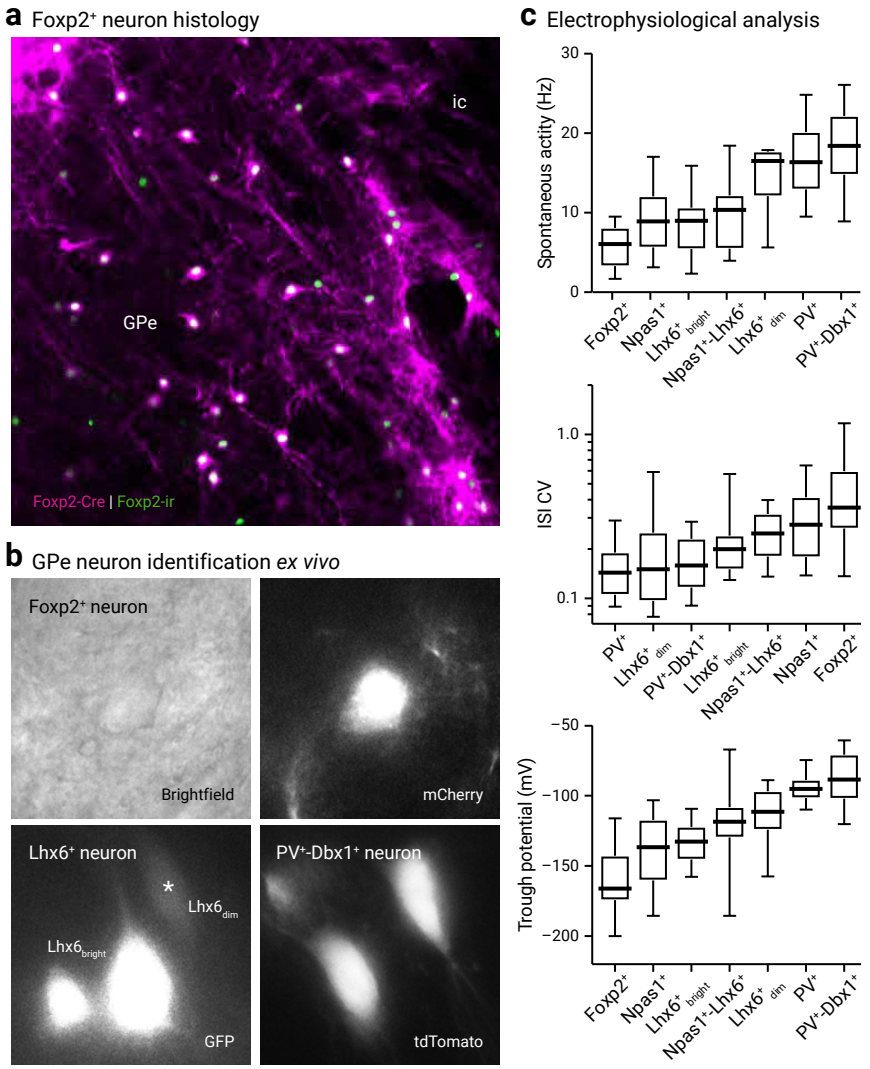

Figure 8

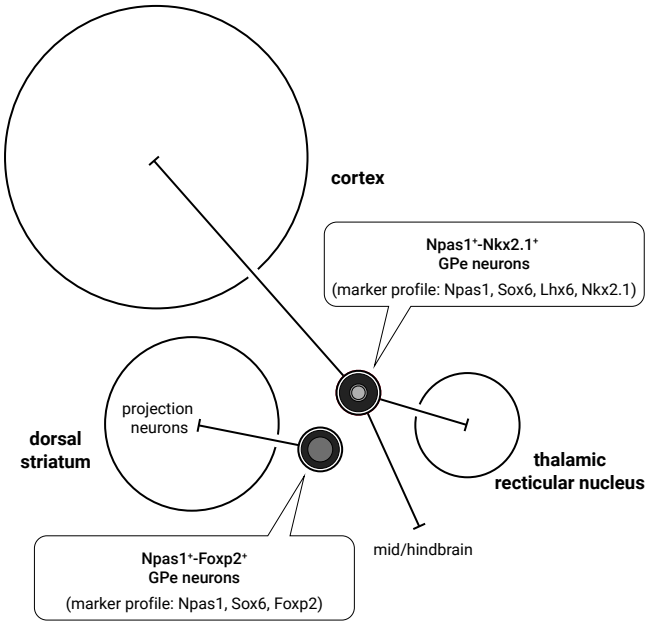

Figure 9

Table 1. Injection coordinates

	Injection volume (nl)	P28–35			P45–55		
		AP (mm)	ML (mm)	DV (mm)	AP (mm)	ML (mm)	DV (mm)
Primary somatosensory, primary somatomotor (MOp, SSp)	180	+2.60	±2.16	−2.55, −2.75	+2.60	±2.16	−2.25, −2.50
Secondary somatomotor (MOs), rostral	180	+1.80	±0.96	−1.20, −1.60	+2.60	±2.04	−2.55, −2.75
Secondary somatomotor (MOs), caudal	–	–	–	–	+1.80	±0.96	−1.20, −1.60
Anterior cingulate cortex (AC)	90	–	–	–	+1.00	±0.40	−1.60
Agranular cortex (AG)	180	+2.25	±1.92	−2.25, −3.00	−2.60	±2.04	−2.55, −2.75
Dorsal striatum (dStr)	180	+0.70	±2.30	−3.00, −3.40	+0.70	±2.30	−3.00, −3.40
External globus pallidus (GPe)	90	−0.28	±2.15	−4.10	−0.28	±2.15	−4.1
Subthalamic nucleus (STN)	90	−1.45	±1.70	−4.52	−1.45	±1.70	−4.53
Substantia nigra (SN)	180	−2.65, −3.00	±1.50	−4.50	−2.95	±1.44	−4.50
Parafascicular nucleus (Pf)	90	−2.1	±0.64	−3.50	−2.15	±0.64	−3.50

Coordinates are in relation to bregma. Negative AP values refers to coordinates caudal to bregma. Abbreviations: AP = anterior-posterior, ML = medial-lateral, DV = dorsal-ventral.

Table 2. Primary antibodies used in this study

Antigen	Host species	Clonality	Source	Catalog no.	Lot. no.	Dilution	Working concentration
ChAT	Gt	Polyclonal	Sigma-Millipore	AB144P	2916187	1:1,000	
ChAT	Rb	Polyclonal	Synaptic Systems	297 013	297013/3	1:2,000	0.5 µg/ml
Cre	Rb	Polyclonal	Synaptic Systems	257003	257003/1–7	1:500	2.0 µg/ml
CTb	Gt	Polyclonal	List Biological Labs	102946-502	7032A10	1:5,000–1:10,000	
DsRed	Rb	Polyclonal	Clontech	632496		1:500–1:1,000	
Foxp2	Ms	Monoclonal	Sigma-Millipore	MABE415	Q2273099	1:500	1.o µg/ml
Foxp2	Rb	Monoclonal	Sigma-Millipore	ABE73	3037985	1:500	
Foxp2	Rb	Polyclonal	Sigma-Millipore	HPA000382	B115858	1:500	
GFP	Ck	Polyclonal	Abcam	ab13970	GR3190550–9	1:1,000	
HuC/D	Ms	Monoclonal	Life Technologies	A21271	1900217	1:1,000	0.2 µg/ml
mCherry	Rt	Monoclonal	Life Technologies	M11217	S1259077	1:1,000–1:5,000	0.4–2.0 µg/ml
NeuN	Rb	Polyclonal	Biosensis	R–3770–100	R-3770-300-201605-SH	1:1,000	1.0 ng/µl
Nkx2.1	Rb	Polyclonal	Sigma-Millipore	07–601	2887266	1:500	
Npas1*	Gp	Polyclonal				1:5,000	
Npas1*	Rb	Polyclonal				1:5,000	
Parvalbumin	Ms	Monoclonal	Sigma-Millipore	P3088	016M-4847V	1:500	10.0 µg/ml
Parvalbumin	Ck	Polyclonal	Synaptic Systems	195 006	195006/2	1:2,000	
Parvalbumin	Gp	Polyclonal	Synaptic Systems	195 004	195 004/1–19	1:1,000–1:2,000	
Parvalbumin	Rb	Polyclonal	Swant	PV 27	2014	1:1,000	
RFP	Ms	Monoclonal	Rockland	200–301–379	34537	1:1,000	0.5 µg/ml
Sox6	Rb	Polyclonal	Abcam	ab30455	GR289554–2	1:5,000	0.2 µg/ml
tdTomato	Rt	Monoclonal	Kerafast	EST203	091918	1:1,000	0.5 µg/ml

*See Hernandez et al. 2015. Abbreviations: Ck = chicken, Gp = guinnea pig, Gt = goat, Ms, Rb = rabbit, Rt = rat.

Table 3. Quantification of GPe neurons

	Sox6$^+$		Nkx2.1$^+$		PV$^+$		Lhx6$^+$		Npas1$^+$		Foxp2$^+$		Dbx1$^+$		ChAT$^+$	
	Median ± MAD	*n* (neurons, sections)	Median ± MAD	*n* (neurons, sections)	Median ± MAD	*n* (neurons, sections)	Median ± MAD	*n* (neurons, sections)	Median ± MAD	*n* (neurons, sections)	Median ± MAD	*n* (neurons, sections)	Median ± MAD	*n* (neurons, sections)	Median ± MAD	*n* (neurons, sections)
Total GPe neurons (%)	63.7 ± 4.0	4,681, 14	59.6 ± 2.3	5,342, 16	49.2 ± 4.3	2,726, 19	33.7 ± 7.5	2,533, 12	32.1 ± 3.9	3,361, 21	22.1 ± 1.1	1,273, 10	9.4 ± 1.2	2,593, 52	5.9 ± 1.7	267, 9
Coexpression (%)																
Sox6	–	–	68.2 ± 0.5	681, 3	52.5 ± 8.4	1,675, 15	75.5 ± 7.2	2,346, 15	93.4 ± 5.6	1,999, 14	67.0 ± 4.3	206, 3	51.6 ± 8.2	442, 15	0 ± 0	0, 3
Nkx2.1	58.2 ± 0.3	681, 3	–	–	83.2 ± 3.5	1,105, 7	78.4 ± 8.0	1,469, 9	32.0 ± 1.4	383, 6	0.0 ± 0.0	1, 3	77.8 ± 10.2	329, 9	–	–
PV	36.4 ± 3.2	1,675, 15	70.8 ± 3.0	1,105, 7	–	–	28.1 ± 7.3	654, 12	2.7 ± 2.7	96, 12	–	–	72.0 ± 8.3	493, 23	–	–
Lhx6	47.0 ± 6.7	2,346, 15	40.6 ± 7.4	1,469, 9	24.1 ± 9.6	654, 12	–	–	40.7± 4.6	818, 12	1.3 ± 1.3	8, 3	–	–	50.0 ± 3.6	48, 3
Npas1	45.4 ± 5.7	1,999, 14	17.3 ± 2.3	383, 6	2.0 ± 2.0	96, 12	35.2 ± 5.1	818, 12	–	–	79.3 ± 3.8	566, 6	9.5 ± 5.2	72, 14	–	–
Foxp2	34.1 ± 5.7	206, 13	0.0 ± 0.0	1, 3	–	–	1.9 ± 0.5	8, 3	56.8 ± 4.2	566, 6	–	–	3.6 ± 1.9	13, 10	–	–
Dbx1	10.4 ± 3.2	411, 15	12.0 ± 1.3	329, 9	13.6 ± 3.0	493, 23	–	–	3.3 ± 1.8	72, 14	1.5 ± 0.6	13, 10	–	–	10.6 ± 4.2	34, 9
ChAT	0.0 ± 0.0	0, 3	–	–	–	–	6.7 ± 0.6	48, 3	–	–	–	–	7.4 ± 3.3	34, 9	–	–

Abbreviation: MAD = median absolute deviation.

Table 4. Quantification of retrogradely-labeled GPe neurons

LVretro-cre	Injection target											
	STN			SN			dStr			Ctx (ORB, MO, SS)		
	Median ± MAD	*n* (neurons)	*n* (sections)	Median ± MAD	*n* (neurons)	*n* (sections)	Median ± MAD	*n* (neurons)	*n* (sections)	Median ± MAD	*n* (neurons)	*n* (sections)
Total tdTomato$^+$	–	750	18	–	127	12	–	406	15	–	293	24
PV$^+$	75.6 ± 6.7	278	9	66.7 ± 26.2	51	9	11.5 ± 4.8	15	6	0.0 ± 0.0	3	8
PV$^-$	20.0 ± 8.7	74	9	28.6 ± 25.3	18	9	88.5 ± 4.8	114	6	100.0 ± 0.0	62	11
Npas1$^+$	15.6 ± 6.5	45	9	15.8 ± 6.4	7	3	75 ± 8.3	200	9	25.0 ± 6.3	41	13
Npas1$^-$	79.1 ± 16.1	247	9	84.2 ± 6.4	51	3	25 ± 8.3	77	9	68.8 ± 11.3	106	13
Npas1$^+$-Nkx2.1$^+$	–	–	–	–	–	–	–	–	–	20.0 ± 6.7	8	3
Nkx2.1$^+$	–	–	–	–	–	–	–	–	–	32.3 ± 5.8	20	6
ChAT$^+$	–	–	–	–	–	–	–	–	–	50.0 ± 0.0	19	3
ChAT$^-$	–	–	–	–	–	–	–	–	–	50.0 ± 0.0	23	3
Foxp2$^+$	–	–	–	–	–	–	–	–	–	0.0 ± 0.0	0	3

CTb	STN			SN			dStr			Ctx (ORB, MO, SS)		
	Median ± MAD	*n* (neurons)	*n* (sections)	Median ± MAD	*n* (neurons)	*n* (sections)	Median ± MAD	*n* (neurons)	*n* (sections)	Median ± MAD	*n* (neurons)	*n* (sections)
Total CTb$^+$	–	592	12	–	173	15	–	42	17	–	116	21
PV$^+$	72.6 ± 11.1	263	9	33.3 ± 11.1	14	9	0.0 ± 0.0	1	8	0.0 ± 0.0	0	3
PV$^-$	27.5 ± 10.6	99	9	66.7 ± 11.1	52	9	100.0 ± 0.0	18	8	100.0 ± 0.0	6	3
Npas1$^+$	6.4 ± 4.4	10	3	18.6 ± 8.3	19	6	100.0 ± 0.0	18	9	40.4 ± 9.7	19	6
Npas1$^-$	93.7 ± 4.4	130	3	81.4 ± 8.3	68	6	0.0 ± 0.0	5	9	60.0 ± 10.0	27	6
Dbx1$^+$	22.6 ± 9.4	94	9	2.2 ± 0.3	20	9	0.0 ± 0.0	0	17	0.0 ± 0.0	0	9
Dbx1$^+$PV$^+$	11.8 ± 11.8	56	9	5.6 ± 5.6	10	15	0.0 ± 0.0	0	8	0.0 ± 0.0	0	3
Dbx1$^+$-PV$^-$	0.0 ± 0.0	7	9	0.0 ± 0.0	6	15	0.0 ± 0.0	0	8	0.0 ± 0.0	0	3
Dbx1$^+$-Npas1$^+$	0.0 ± 0.0	0	3	0.0 ± 0.0	2	9	0.0 ± 0.0	0	9	0.0 ± 0.0	0	6
Dbx1$^+$-Npas1$^-$	14.6 ± 2.1	27	3	0.0 ± 0.0	6	9	0.0 ± 0.0	0	9	0.0 ± 0.0	0	6

Abbreviations: STN = subthalamic nucleus, SN = substantia nigra, dStr = dorsal striatum, Ctx = cortex, ORB = orbital area, MO = somatomotor area, SS = somatosensory area, MAD = median absolute deviation.

Table 5. Electrophysiological characteristics of GPe neurons

	PV^+		$Npas1^+$		$Foxp2^+$		$Lhx6^+$		$Lhx6^+_{dim}$		$Lhx6^+_{bright}$		$Dbx1^+$		$Dbx1^+$-PV^+		$Npas1^+$-$Lhx6^+$	
	Median ± MAD	*n**	Median ± MAD	*n*	Median ± MAD	*n*	Median ± MAD	*n*	Median ± MAD	*n*	Median ± MAD	*n*	Median ± MAD	*n*	Median ± MAD	*n*	Median ± MAD	*n*
Firing rate (Hz)	16.69 ± 3.43	111	8.17 ± 3.26	62	6.07 ± 1.91	20	10.6 ± 5.12	42	16.53 ± 1.15	7	9.48 ± 1.71	17	13.2 ± 2.66	21	18.42 ± 3.62	16	10.36 ± 2.83	14
ISI CV	0.14 ± 0.04	87	0.26 ± 0.09	62	0.36 ± 0.09	19	0.21 ± 0.07	42	0.15 ± 0.07	7	0.2 ± 0.04	16	0.14 ± 0.02	20	0.16 ± 0.05	16	0.25 ± 0.07	14
Max rate (Hz)	198 ± 24	49	94 ± 34	32	55 ± 23	16	115 ± 33	46	162 ± 16	9	102 ± 32	21	180 ± 27	24	164 ± 30	21	–	–
Max Current (pA)	1140 ± 260	49	230 ± 150	32	160 ± 60	13	345 ± 205	46	860 ± 360	9	320 ± 180	21	880 ± 250	24	700 ± 300	21	–	–
Trough Potential (mV)	−96.08 ± 7.02	74	−147.4 ± 16.57	44	−166.05 ± 7.57	16	−121.75 ± 16.15	60	−111.34 ± 10.47	9	−132.5 ± 12.31	21	−104.26 ± 8.57	24	−88.42 ± 16.32	21	−118.53 ± 10.5	16
Sag ratio	1.1 ± 0.03	41	1.24 ± 0.14	44	1.33 ± 0.13	16	1.14 ± 0.07	60	1.14 ± 0.04	9	1.21 ± 0.09	21	1.14 ± 0.07	24	1.13 ± 0.08	21	1.06 ± 0.04	16
First/last ISI ratio	0.73 ± 0.05	26	0.61 ± 0.05	32	0.63 ± 0.06	16	0.67 ± 0.06	46	0.67 ± 0.04	9	0.66 ± 0.07	21	0.71 ± 0.07	24	0.69 ± 0.03	21	–	–
First AP height (mV)	61.89 ± 4.3	18	63.4 ± 8.61	23	66.57 ± 8.47	16	63.3 ± 7.89	32	61.84 ± 4.92	10	64.48 ± 7.43	21	63.87 ± 4.24	24	59.78 ± 3.14	21	–	–
FWHM (ms)	0.67 ± 0.05	18	1.11 ± 0.24	23	1.24 ± 0.33	16	0.95 ± 0.16	32	0.74 ± 0.08	10	1 ± 0.18	21	0.7 ± 0.06	24	0.77 ± 0.12	21	–	–

* *n* = neurons. Abbreviations: MAD = median absolute deviation, ISI = interspike interval, CV = coefficient of variation, AP = action potential, FWHM = full width at half maximum.

Table 6. Statistical analysis for electrophysiological characteristics

	Pairwise comparisons, Mann-Whitney *U* test*																
	PV^+ vs PV^+-$Dbx1^+$	PV^+ vs $Npas1^+$	PV^+ vs $Lhx6^+$	PV^+ vs $Foxp2^+$	PV^+ vs $Dbx1^+$	$Npas1^+$ vs $Lhx6^+$	$Npas1^+$ vs $Foxp2^+$	$Npas1^+$ vs $Dbx1^+$	$Npas1^+$ vs PV^+-$Dbx1^+$	$Foxp2^+$ vs $Lhx6^+$	$Lhx6^+$ vs $Dbx1^+$	$Lhx6^+$ vs PV^+-$Dbx1^+$	$Fox2^+$ vs $Dbx1^+$	$Fox2^+$ vs PV^+-$Dbx1^+$	$Dbx1^+$ vs PV^+-$Dbx1^+$	$Lhx6^+_{bright}$ vs PV^+	$Lhx6^+_{bright}$ vs $Npas1^+$
Firing rate	0.2829	<0.0001	<0.0001	<0.0001	0.0011	0.1096	0.0122	0.0008	<0.0001	0.0009	0.1897	0.0005	<0.0001	<0.0001	0.0015	<0.0001	0.8341
ISI CV	0.5739	<0.0001	<0.0001	<0.0001	0.7350	0.0591	0.0453	<0.0001	0.0004	0.0009	0.0038	0.0460	<0.0001	<0.0001	0.7953	0.0046	0.1302
Max rate	0.0114	<0.0001	<0.0001	<0.0001	0.2864	0.0593	0.0447	<0.0001	<0.0001	0.0003	<0.0001	0.0007	<0.0001	<0.0001	0.2602	<0.0001	0.8431
Max current	0.0004	<0.0001	<0.0001	<0.0001	0.0051	0.0338	0.0470	<0.0001	<0.0001	0.0002	0.0004	0.0047	<0.0001	<0.0001	0.4806	<0.0001	0.3706
Trough potential	0.1078	<0.0001	<0.0001	<0.0001	0.0008	<0.0001	0.0144	<0.0001	<0.0001	<0.0001	0.0017	<0.0001	<0.0001	<0.0001	0.0020	<0.0001	0.1096
Sag ratio	0.3366	<0.0001	<0.0001	<0.0001	<0.0001	0.2113	0.0046	0.9908	0.0174	<0.0001	0.3417	0.0961	0.0065	<0.0001	0.0540	<0.0001	0.1287
First/last ratio	<0.0001	<0.0001	<0.0001	<0.0001	0.0120	0.0010	0.3600	0.0002	0.0005	0.0838	0.2355	0.7349	0.0250	0.0312	0.4396	0.0005	0.0141
First AP height	0.2816	0.5940	0.5956	0.1347	0.7918	0.9798	0.2752	0.6351	0.1217	0.3024	0.6514	0.1393	0.1827	0.0193	0.2007	0.3211	0.7624
FWHM	0.0832	<0.0001	<0.0001	<0.0001	0.3674	0.0802	0.1138	<0.0001	<0.0001	0.0074	0.0001	0.0012	<0.0001	<0.0001	0.5021	<0.0001	0.4702

(Cont'd)

	Lhx6$^{+}_{bright}$ vs Foxp2^{+}	Lhx6$^{+}_{bright}$ vs PV^{+}-Dbx1^{+}	Lhx6$^{+}_{bright}$ vs Dbx1^{+}	Lhx6$^{+}_{dim}$ vs PV^{+}	Lhx6$^{+}_{dim}$ vs Npas1^{+}	Lhx6$^{+}_{dim}$ vs Foxp2^{+}	Lhx6$^{+}_{dim}$ vs PV^{+}-Dbx1^{+}	Lhx6$^{+}_{dim}$ vs Dbx1^{+}	Lhx6$^{+}_{bright}$ vs Lhx6$^{+}_{dim}$	Npas1-Lhx6^{+} vs Lhx6$^{+}_{bright}$	Npas1^{+}-Lhx6^{+} vs Lhx6$^{+}_{dim}$	Npas1^{+}-Lhx6^{+} vs PV^{+}	Npas1^{+}-Lhx6^{+} vs Npas1^{+}	Npas1^{+}-Lhx6^{+} vs Foxp2^{+}	Npas1^{+}-Lhx6^{+} vs Dbx1^{+}	Npas1^{+}-Lhx6^{+} vs PV^{+}-Dbx1^{+}
Firing rate	0.0389	<0.0001	0.0051	0.4596	0.0114	0.0004	0.1750	0.1927	0.0076	0.3391	0.0200	<0.0001	0.3777	0.0026	0.0713	0.0005
ISI CV	0.0035	0.0865	0.0103	0.7384	0.0591	0.0112	0.9862	0.7578	0.4127	0.3338	0.1490	0.0004	0.6056	0.0204	0.0025	0.0060
Max rate	0.0277	<0.0001	<0.0001	0.0275	<0.0001	<0.0001	0.9381	0.3966	<0.0001	–	–	–	–	–	–	–
Max current	0.0108	0.0008	<0.0001	0.0681	<0.0001	<0.0001	0.7734	0.2876	0.0005	–	–	–	–	–	–	–
Trough potential	0.0009	<0.0001	<0.0001	0.0034	0.0015	0.0003	0.0050	0.3916	0.0113	0.0304	0.4523	<0.0001	0.0031	0.0012	0.0952	0.0012
Sag ratio	0.0537	0.0009	0.1313	0.0164	0.4306	0.0008	0.3722	0.3282	0.0279	<0.0001	0.0981	0.6255	0.0024	<0.0001	0.0038	0.5750
First/last ratio	0.1951	0.6494	0.3173	0.0002	0.0112	0.1210	0.6646	0.2753	>0.9999	–	–	–	–	–	–	–
First AP height	0.5544	0.0872	0.3257	0.9812	0.8323	0.2625	0.4409	0.7520	0.5463	–	–	–	–	–	–	–
FWHM	0.0507	<0.0001	<0.0001	0.0208	0.0058	0.0034	0.4921	0.1565	0.0132	–	–	–	–	–	–	–

*Two-tailed *P* values are listed. Abbreviations: MAD = median absolute deviation.